p38MAPKα stromal reprogramming sensitizes metastatic breast cancer to immunotherapy

Douglas V. Faget[1], **Xianmin Luo**[1], **Matthew J. Inkman**[2], **Qihao Ren**[1], **Xinming Su**[3], **Kai Ding**[4,5,8], **Michael R. Waters**[2], **Ganesh Kumar Raut**[1], **Gaurav Pandey**[2], **Paarth B. Dodhiawala**[3,6,14], **Renata Ramalho-Oliveira**[1], **Jiayu Ye**[1], **Thomas Cole**[1], **Bhavna Murali**[1], **Alexander Zheleznyak**[2], **Monica Shokeen**[2,7], **Kurt R. Weiss**[10], **Joseph B. Monahan**[9], **Carl J. DeSelm**[2], **Adrian V. Lee**[4,5,11], **Steffi Oesterreich**[4,5,11], **Katherine N. Weilbaecher**[1,3,12,15], **Jin Zhang**[2,13,15], **David G. DeNardo**[3,12,14,15], **Sheila A. Stewart**[1,3,14,15,#]

[1]Department of Cell Biology and Physiology, Washington University School of Medicine, St Louis, MO

[2]Department of Radiation Oncology, Washington University School of Medicine, St Louis, MO

[3]Department of Medicine, Washington University School of Medicine, St Louis, MO

[4]Womens Cancer Research Center, UPMC Hillman Cancer Center, Pittsburgh, PA

[5]Magee-Womens Research Institute, Pittsburgh, PA

[6]Medical Scientist Training Program, University of Minnesota Medical School, Minneapolis, MN

[7]Department of Biomedical Engineering, Washington University School of Medicine, St Louis, MO

[8]Integrative Systems Biology Graduate Program, University of Pittsburgh, Pittsburgh, PA

[9]Aclaris Therapeutics, St Louis, MO

[10]Department of Orthopaedic Surgery, University of Pittsburgh, Pittsburgh, PA

[11]Department of Pharmacology and Chemical Biology & Department of Human Genetics, University of Pittsburgh, Pittsburgh, PA

[12]Department of Pathology and Immunology, Washington University School of Medicine, St Louis, MO

[13]Institute for Informatics (I^2), Washington University School of Medicine, St Louis, MO

[14]ICCE Institute, Washington University School of Medicine, St Louis, MO

[15]Siteman Cancer Center, Washington University School of Medicine, St Louis, MO

Abstract

[#]**Corresponding Author**: Sheila A. Stewart, Department of Cell Biology and Physiology, Washington University School of Medicine, 660 South Euclid Avenue, Campus Box 8228, St. Louis, MO 63110. Phone: 314-362-7449; Fax: 314-362-7463; sheila.stewart@wustl.edu.

Metastatic breast cancer is an intractable disease that responds poorly to immunotherapy. We show that p38MAPKα inhibition (p38i) limits tumor growth by reprograming the metastatic tumor microenvironment in a CD4+ T cell, IFNγ, and macrophage dependent manner. To identify targets that further increased p38i efficacy, we utilized a stromal labeling approach and single cell RNA sequencing. Thus, we combined p38i and an OX40 agonist that synergistically reduced metastatic growth and increased overall survival. Intriguingly, patients with a p38i metastatic stromal signature had better overall survival that was further improved by the presence of an increased mutational load, leading us to ask if our approach would be effective in antigenic breast cancer. The combination of p38i, anti-OX40, and cytotoxic T cell engagement cured mice of metastatic disease and produced long-term immunologic memory. Our findings demonstrate that a detailed understanding of the stromal compartment can be used to design effective anti-metastatic therapies.

Introduction

Despite initial success in limiting disease progression, current cancer therapy agents often fail to control metastatic breast tumors and patients succumb to their disease (1). Currently, most antitumor agents directly target tumor cells, neglecting the surrounding stroma. The metastatic tumor microenvironment (TME) provides shelter to disseminated tumor cells from immune response and chemotherapy (2, 3). Hence, effective anti-metastatic therapy requires a more thorough understanding of the mechanisms by which the TME supports metastatic breast cancer growth and how they can be targeted to improve breast cancer therapy.

The metastasis-associated stroma is remarkably distinct from the stroma found in primary tumors (2, 4, 5) and may represent an untapped therapeutic target. Human metastatic breast cancer lesions often show increased macrophage infiltration and reduced T cell recruitment in comparison to patient-matched primary tumors, suggesting an increased immunosuppressive environment in breast cancer metastases (5). Indeed, the metastatic sites are characterized by a distinct tumor immunity. A recent study evaluated the response to immune checkpoint therapy (ICT) in different TMEs in a prostate cancer mouse model. They found that the subcutaneous TME was characterized by a Th1-CD4+ T cell response that could reduce tumor growth when treated with ICT, while the bone TME displayed an increased Th17 response that failed to impact tumor growth under the same treatment conditions (2). Together, these studies highlight the astonishing differences that exist between the metastatic and primary tumor stroma that can drive vastly different responses to therapy.

The tumor stroma is a harsh environment often characterized by conditions, such as oxidative stress, chronic inflammation, and senescence (6, 7) that activate stress-induced kinases including p38MAPK (p38) within the TME (8). In addition, tumor-derived

factors have been shown to drive p38 activation in stromal cells, such as fibroblasts and macrophages (9, 10). Our group has shown that inhibition of the p38 pathway can limit cancer associated fibroblasts (CAF)-mediated tumorigenesis (11). More recently, p38MAPKα (p38α) activation in fibroblasts from the pre-metastatic niche was shown to support tumor colonization and growth in the lungs in murine melanoma models (9). In addition, we found that p38α regulates a plethora of pro-tumorigenic and inflammatory factors in the tumor stroma of human breast tumors and its inhibition limits metastatic growth in murine breast tumor models (12). However, it remains unclear how stromal p38α signaling shapes the metastatic TME and affects tumor immunity in metastatic breast cancer.

Here, we sought to determine how the stromal p38α pathway supports breast metastases and how we could leverage this information to further enhance current cancer therapy for patients with metastatic breast cancer. We found that pharmacological targeting or genetic ablation of p38α in hematopoietic stromal cells restrained metastatic tumor growth in several breast cancer mouse models. Next, we used a recently developed approach to label the tumor-associated niche in bone metastases to identify mechanisms by which stromal p38α activation supports metastatic tumor growth. We found that p38α inhibition limited differentiation of immunosuppressive macrophages, allowing an increase in CD4^{+} T cell-mediated immune responses. Transcriptomic analyses revealed specific gene signatures associated with p38α inhibition that predicted breast cancer patients' outcome. We leveraged our transcriptomic findings that revealed that Tnfsf4 (i.e., OX40L) was poorly expressed in the TME of bone metastases to enhance immunotherapy response by combining agonist anti-OX40 with p38α inhibition in clinically relevant metastasis mouse models. Finally, interrogation of human data revealed that breast cancer patients with a higher p38i stromal signature had better overall survival that was further increased in patients with high tumor mutational burden. Thus, we provided an experimental antigen and found that the combination of p38α inhibition and anti-OX40 led to a curative response and immunologic memory.

Results

Inhibition of p38α signaling limits metastatic tumor growth

We previously reported that p38α-dependent pro-tumorigenic stromal factors are overexpressed in human breast tumors and that pharmacological inhibition of p38α (p38i) reduced metastatic growth in visceral organs and bones (12). Accordingly, phosphorylated p38α or MK2, its downstream target, was detected in the stroma of human breast metastases found in different organs (Fig. 1A). However, the cells targeted by p38i and the mechanisms by which stromal p38α signaling supports metastatic tumors remain poorly understood. To investigate whether the pro-tumorigenic role of stromal p38 signaling was restricted to metastatic breast tumor growth, we first evaluated whether pharmacological inhibition of p38α signaling impacted primary tumor growth and subsequent metastasis. To test this, PyMT-BO1 breast tumor cells (Luminal B) were orthotopically implanted and mice were randomized to a control or treatment group. The treatment group received a clinically available and selective p38α inhibitor – CDD-111 (formerly named SD0006 (13); hereafter referred to as p38i) – compounded into mouse chow and administered *ad libitum*. Tumors

were allowed to grow for 3 weeks in the presence or absence of p38i at which time the mice underwent mastectomy and metastasis incidence was measured 4 weeks later (Fig. 1B). While p38i had no impact on primary tumor growth or local recurrence (Fig. 1C, 1D), it limited the incidence of detectable metastases throughout the body from 75% in the control group to 36% in the p38i treatment group (Fig. 1D). The organs affected by spontaneous metastases in this model include the lungs, liver, kidneys, and bones (Fig. S1A). These results suggest stromal p38α signaling controls the dissemination and/or outgrowth of breast tumor metastases.

Bone is one of the most common sites of human breast cancer metastasis (1), but murine primary tumor models rarely develop bone metastasis. Indeed, we achieved a low rate of spontaneous bone metastases, ranging from 9 to 16% of total mouse cohorts (Fig. S1A). Grounded in our findings that p38i limited spontaneous metastasis to both the bone and visceral organs (Fig. 1D), we delivered tumor cells through intracardiac (i.c.) injection into the left ventricle to induce reliable widespread metastases including in the bone (Fig. 1E). Following i.c. injection of tumor cells, mice were randomized to vehicle or p38i-compounded chow. As we have previously shown, p38i limited metastatic tumor growth of PyMT-BO1 cells by ≈2.4-fold in multiple organs (Fig. 1F), including the bone where growth was reduced to a similar rate (Fig. 1G). Importantly, the antitumor effects of p38i were not limited to young mice. When PyMT-BO1 cells were implanted into 18/19-month old mice (≈55/60-year old human), p38i was as effective at limiting tumor growth as when treating 7-week old mice (Fig. S1B, 1F). Given the vast majority of breast cancer patients are older, this finding has important clinical implications. Finally, the antitumor effect of p38i was consistent across several breast tumor cell lines and mouse strains. We found that p38i limited the metastatic growth of EO771 (Luminal B), NT2.5 (HER2+) and EMT6 (Triple-negative) breast tumor models by ≈2.3-, ≈4.1-, and ≈82-fold, respectively (Fig. 1H, 1I, 1J). Thus, targeting p38α signaling significantly reduces metastatic breast cancer tumor growth in several mouse models that represent distinct human breast cancer subtypes.

Hematopoietic p38α supports metastatic tumor growth

The p38MAPK pathway plays a pivotal role in inflammatory responses, impacting innate and adaptive immune cells (8, 14–16) and we have shown it reduces metastatic tumor growth by targeting the stromal compartment (12). However, whether p38α signaling in the immune stroma contributes to metastatic tumor growth remains an open question. Hence, we sought to determine whether deletion of *Mapk14* (i.e., p38MAPKα) in the hematopoietic stromal compartment recapitulated the effect of p38i in reducing bone metastatic tumor growth. To assess this hypothesis, we interbred the *Mapk14*fl/fl mouse strain with a ubiquitous tamoxifen-inducible Cre-expressing (UBC-CreERT2) and a tdTomato Cre-reporter (Ai14) strains to generate UBC-CreERT2Tg/0*Mapk14*fl/flAi14LSL/LSL (Cre+) and *Mapk14*fl/flAi14LSL/LSL (Cre-) mice (Fig. S1C). Then, we performed bone marrow transplantation from Cre+ and Cre- CD45.2 littermate donors into lethally irradiated wildtype CD45.1 B6 mice. Animals were allowed to recover in the absence of CreERT2 activation, retaining wild-type expression of p38α during the six-week recovery period (Fig. 1K, 1L). CD45.1 B6 recipient mice were then treated with tamoxifen-compounded chow for a week to activate CreERT2. Using this approach, we routinely achieved greater than

90% chimerism (Fig. S1D) and greater than 80% of CreER[T2] activation, as confirmed by the frequency of CD45.2+ and TdTomato+ (TdT) cells in the blood of transplanted mice (Fig. S1E), respectively. Further, p38α deletion was confirmed by western blot analysis of bone marrow protein content after tamoxifen treatment (Fig. S1F). After a one-week washout period (Fig. 1K), PyMT-BO1 cells were implanted by i.c. injection and tumor growth in the bone was assessed after two weeks. p38α can impact osteoclastogenesis (17), which is known to impact tumor cell seeding in the bone (1). However, in our model, we found that deleting p38α in hematopoietic cells one week prior to tumor cell implantation had no impact on bone density or tumor cell seeding (Fig. S1G, S1H). Finally, we found that deletion of p38α in hematopoietic cells, similar to pharmacologic inhibition of p38α, reduced metastatic tumor growth in visceral organs and in the bone (Fig. 1M, 1N). These data indicate that p38α signaling in the hematopoietic compartment supports metastatic tumor growth.

Inhibition of p38α shifts macrophage phenotype in bone metastases

The reduction in bone metastatic growth observed upon *Mapk14* knockout in hematopoietic cells (Fig. 1N) led us to investigate how p38i shapes the tumor immune microenvironment within a metastatic bone lesion. Recent work has underscored the importance of analyzing tumor site-specific immune cells (2), however, the bone marrow presents a unique challenge to studying tumor-associated immune cells. Indeed, the majority of immune cells within the bone are not associated with a metastatic lesion. To overcome this issue, we took advantage of a recently developed strategy to label tumor proximal stromal cells. Ombrato and colleagues demonstrated that the addition of a lipid-soluble tag to the mCherry protein (sLPmCherry) allows the labeling of proximal cells that are located up to 100μm from sLPmCherry-producing tumor cells (18). To make use of this system, we modified PyMT-BO1 cells to express sLPmCherry (PyMT-BO1-sLPmCher) (Fig. 2A). Next, we implanted PyMT-BO1-sLPmCher cells through i.c. injection and treated mice as shown in Fig. 1E. At day 13, femurs were isolated from control or p38i-treated mice, crushed and digested with collagenase to make single cell suspensions. Cellular suspensions were stained with anti-CD45 and the CD45+mCherry- and CD45+mCherry+ populations were sorted and submitted for single cell RNA sequencing (scRNAseq) (Fig. S2A). Using this strategy, we identified tumor-associated lymphoid and myeloid immune cells that were proximal (mCherry+) and distal (mCherry-) to the bone metastases (Fig. 2B, S2B, S2C). Analysis of the myeloid clusters revealed a considerable increase in two populations within the proximal stroma, myeloid antigen-presenting cells (myeloid APCs) and basophils. The myeloid APC cluster consisted primarily of macrophages and a few dendritic cells, as evidenced by expression of Cd68 and Zbtb46, respectively (Fig. S2D). We next analyzed the transcriptome differences between myeloid APCs under vehicle versus p38i treatment. We observed that markers associated with tumor-promoting macrophages (M2-like) were downregulated in the p38i group (e.g., Arg1; Ecm1; Fn1; Spp1), while markers associated with tumor-suppressive macrophages (M1-like) were upregulated, such as MHCII genes and other interferon-responsive genes (e.g., Slamf8; Cxcl9; H2-Aa; H2-Ab1; Stat1) (Fig. 2C, 2D, 2E). Indeed, gene set enrichment analyses revealed increased IFNγ and adaptive immune response signatures in myeloid APCs from p38i-treated mice (Fig. 2F). Next, a similar approach was used to analyze the non-immune stroma in the same metastatic lesions

(Fig. S2E, S2F). These analyses revealed other stromal cell types in proximity with tumor cells, such as CAFs and endothelial cells that also showed an augmented IFNγ response signature upon p38i treatment (Fig. S2G). Next, we performed histological analyses to validate the scRNAseq findings. These analyses confirmed that bone metastases were highly infiltrated by macrophages (Fig. 2G), and that p38i treatment increased MHCII stained area from ≈5% to ≈15% and decreased ARG1 stained area from ≈1.3% to ≈0.4% (Fig. 2H, 2I) in bone metastases, corroborating the scRNAseq data (Fig. 2E). Flow cytometry analyses also confirmed that tumor-associated macrophages (mCherry+) showed higher MHCII expression when compared to bystander bone macrophages (mCherry-) under p38i treatment, as evidenced by a 40% increase on average in the mean fluorescence intensity for MHCII staining (Fig. 2J). Consistent with these results we found that the lack of *Mapk14* in hematopoietic cells increased MHCII stained area from ≈5% to ≈18% and decreased ARG1 stained area from ≈0.42% to ≈0.15% in bone metastases shown in Fig. 1N (Fig. 2K, 2L). Collectively, these data indicate that limiting p38α activity in the metastatic setting shifted macrophages towards a tumor-suppressive phenotype.

Our scRNAseq analyses revealed the appearance of putative tumor-suppressive macrophages upon p38i (Fig. 2B, 2C, 2D, 2E) and extensive evidence of IFNγ pathway activation in the tumor microenvironment (Fig. 2F, S2G). IFNγ can stimulate several antitumor mechanisms including macrophage-mediated killing of tumor cells (19). To assess whether macrophages could kill PyMT-BO1 tumor cells upon IFNγ stimulation, we admixed tumor cells with tumor-associated (mCherry+) macrophages obtained from untreated mice. Indeed, we found that when exposed to LPS and IFNγ, they effectively restrained PyMT-BO1 tumor cell proliferation whereas unstimulated macrophages failed to do so (Fig. S3A, S3B). It is important to highlight that while we observed many dead cells upon LPS and IFNγ stimulation (Fig. S3B), we cannot rule out macrophage-mediated cytostatic control of PyMT-BO1 tumor cells. This result raised the possibility that macrophages played a central role in controlling metastatic tumor growth, although p38i was not able to further enhance macrophage-mediated killing upon stimulation *in vitro* (Fig S3C, S3D). To address this possibility, we depleted macrophages from mice by using a combination of anti-CSF1 blocking antibody and clodronate liposomes leading to a greater than 90% reduction in macrophages within the bone (Fig. S3E). Upon successful macrophage depletion, PyMT-BO1 cells were implanted through i.c. injection. In this setting, p38i failed to decrease metastatic tumor growth compared to control animals (Fig. 2M). Importantly, p38i remained effective at reducing metastatic tumor growth in mice treated with an isotype antibody control and PBS liposomes (Fig.S3F, S3G). Together these findings indicate that macrophages are necessary to mediate the antitumor activities of p38i.

p38-dependent gene signature from tumor-associated macrophages predicts worse overall survival in patients with breast cancer

Our scRNAseq findings showed that p38i treatment limited a tumor-promoting macrophage gene signature that included immunosuppressive genes in metastasis-bearing mice and induced an IFNγ response signature in different tumor stroma cell types (Fig. 2D, 2E, 2F, S2G). The downregulation of genes associated with tumor-promoting macrophages (e.g., Arg1; Spp1; Fn1) upon p38α inhibition suggests that the p38MAPK pathway is an

important regulator of macrophage polarization. To address this hypothesis, we stimulated bone marrow-derived macrophages (BMM) from the ARG1 reporter mice (YARG) with polarizing cytokines in the presence or absence of p38i. The impact on macrophage polarization was analyzed by assessing ARG1 reporter gene (YFP) and MHCII expression levels by flow cytometry. First, we observed that p38i had no impact on the frequency of MHCII+ BMMs in response to IFNγ (Fig. 3A), indicating that the increased MHCII expression levels found in the mouse model were not due to a direct effect of p38i on macrophages (Fig. 2H, 2J). Next, we found that p38i reduced the frequency of ARG1+ BMMs in a dose-dependent manner in response to IL4 and IL13, further indicating that the p38α pathway controls M2 macrophage polarization and Arg1 expression (Fig. 3B, Fig. S4A). Indeed, these findings are in accordance with previously published studies that have implicated p38 signaling in macrophage polarization towards a tumor-promoting phenotype in other cancer models (10, 16). Collectively, these data suggest that the downregulated gene signature found in tumor associated macrophages (TAMs) upon p38i treatment (Fig. 2D) is dependent on p38 pathway.

We previously found that the expression of p38-dependent factors is present in the stromal compartment of primary breast cancer patients (12). Moreover, we found a significant positive correlation between the 'p38-dependent' macrophage gene signature we uncovered (Fig. 2D, S4B, S4C) and the stroma-derived prognostic predictor (SDPP) signature described by Finak et al. (20) in human breast cancer samples from The Cancer Genome Atlas (TCGA) (Fig. S4D). Next, we used the TCGA database to assess whether this p38-dependent signature had predictive value for patient outcome in a larger cohort. Luminal B and basal-like human breast cancer patients with high expression of the p38-dependent gene signature had worse overall survival in comparison to patients with low expression of the same signature (Fig. 3C, 3D). Since the TCGA database is composed of primary tumor samples, we next sought to determine whether the p38-dependent macrophage signature could also be found in human bone metastases. To assess this hypothesis, we used scRNAseq data obtained from 4 different bone metastases (BoM) from 3 different patients with breast cancer. Endothelial cells, epithelial cells, fibroblasts, osteoclasts and immune cells including myeloid cells, such as monocytes and macrophages, were recovered in the BoM samples. Cell types were assigned based on the expression of canonical cell markers and SingleR (Fig. S4E, S4F). No major batch effect was observed as cells were clustered based on their types rather than sample of origin. The scRNAseq analyses revealed that myeloid cells in bone metastases showed higher levels of the p38-dependent gene signature when compared to epithelial, endothelial and other immune cell types (Fig. 3E, 3F). Together, these data show that the p38-dependent macrophage gene signature is associated with a worse overall survival of human breast cancer patients and it is present in myeloid cells from metastatic lesions in the bone.

Limiting p38α signaling triggers a Th1 CD4+ T cell response in metastasis-bearing mice

The observed enrichment of the IFNγ response signature in tumor-associated stromal cells after p38i treatment (Fig. 2F, S2G) led us to investigate whether IFNγ played a role in the antitumor activities of p38i. To address this hypothesis, IFNγ was blocked starting two days prior to tumor cell implantation with additional injections of the neutralizing antibody every

four days and p38i treatment was started as before (Fig. 1E). IFNγ neutralization completely reversed the antitumor effects of p38i (Fig. 4A), indicating that IFNγ secretion is required to decrease metastatic tumor growth upon p38i treatment.

IFNγ is a key antitumor cytokine that is largely secreted by NK cells, Th1 and cytotoxic T cells (19). Hence, we hypothesized that other immune cell types could contribute to p38i's antitumor effects by secreting IFNγ. To address this question, we first used antibodies to deplete NK cells in metastasis-bearing mice. Although NK cell depletion significantly increased tumor burden in comparison to mock control animals by ≈2-fold, p38i retained the ability to restrain metastatic tumor growth in the absence of NK cells (Fig. S5A). B cells can limit tumor progression typically through antibody dependent cellular cytotoxicity (ADCC) (reviewed in (21)) and can produce IFNγ in non-tumor settings (22). To address whether B cells contributed to the antitumor effects of p38i, we i.c. implanted PyMT-BO1 cells in a B-cell deficient mouse background (mutMt-) and treated mice as shown in Fig 1E. Despite a robust B cell deficiency, we found that p38i still reduced metastatic growth (Fig. S5B), indicating that B cells were dispensable for the antitumor effects of p38i.

Next, we turned our attention to T cells and found that the combined antibody depletion of CD4$^+$ and CD8$^+$ T cells completely abrogated p38i's antitumor effect in mice bearing metastatic breast tumors (Fig. 4B). The requirement for T cells in this setting was further confirmed in a T-cell deficient mouse model (Tcra–/–) where we found that p38i completely failed to limit metastatic breast cancer growth throughout the body and in the bones (Fig. 4C, S5C). Next, to delineate whether it was CD4$^+$ and/or CD8$^+$ T cells that contributed to p38i's antitumor effect, we single depleted helper or cytotoxic T cells using anti-CD4 or anti-CD8 antibodies, respectively. Surprisingly, CD8$^+$ T cell depletion had no impact on p38i-mediated reduction of metastatic growth (Fig. 4D). In contrast, CD4$^+$ T cell depletion reversed the antitumor effect of p38i (Fig. 4D). In addition, p38i did not reduce metastatic tumor growth throughout the body nor in the bones in a CD4$^+$ T cell-deficient mouse model (MHCII-/-) (Fig. 4E, S5D). Together, these data show that helper CD4$^+$ T cells are required to limit metastases upon p38α inhibition.

The involvement of helper T cells in reducing metastatic tumor growth after p38i treatment led us to investigate how inhibition of p38α shapes T cell identity and function in the bone. Although we identified a T cell cluster in our mouse scRNAseq dataset (Fig. S2B), too few metastasis-associated T cells (mCherry+) were recovered to analyze. Hence, we first assessed T cell phenotypes in the bone using histological and cytometry approaches. Our histological analyses of tumor-bearing bones from p38i treated mice revealed increased CD4+ and CD8$^+$ T cell infiltration in bone metastases, suggesting that the requirement of CD4+ T cells is partially explained by increased helper T cell recruitment (Fig. 4F, 4G). Next, we isolated femur bones of tumor-bearing mice from the control group and p38i-treated group and analyzed T cells by flow cytometry. We found that around 42% of CD4$^+$ T cells were activated (CD62L$^-$CD44$^+$) in mice from the p38i-treated group in comparison to 24% in control mice, while no significant increase in the frequency of activated CD8$^+$ T cells was observed (Fig. 4H). Accordingly, we also found increased frequency of PD-1$^+$ CD4$^+$ T cells in the bones of p38i-treated mice in comparison to control, whereas, no relevant increase in the percentage of PD-1$^+$ CD8$^+$ T cells was observed (Fig.

S5E). Together these data corroborate the increased activation profile of CD4$^+$ T cells upon p38i treatment.

Using the PyMT-BO1-sLPmCher cell line to label metastasis-associated T cells, we found that mCherry+ (metastasis-associated) CD4$^+$ T cells showed higher activation in comparison to mCherry- (bystander) CD4$^+$ T cells in both vehicle and p38i-treated animals (Fig. 4I). We observed that an average of 42% of total bystander CD4$^+$ T cells were activated versus 56% of total metastasis-associated CD4$^+$ T cells in p38i-treated group, while the same populations showed 24% and 33% of activation in the vehicle group, respectively (Fig. 4I). Furthermore, the frequency of activated metastasis-associated CD4$^+$ T cells was significantly higher under p38i treatment in comparison to vehicle (Fig. 4I). CD4$^+$ T cells can differentiate into different subtypes, such as Th1, Th2, Th17 and Treg. Among these four classical subtypes, Th1 lymphocytes, which are characterized by high levels of IFNγ secretion, play potent antitumor roles in many contexts (23). Hence, we assessed whether CD4$^+$ T cells from p38i-treated mice produced more IFNγ. To assess the capacity of CD4$^+$ T cells to produce IFNγ, we isolated total splenocytes from tumor-bearing mice treated with p38i or vehicle and stimulated with PMA and ionomycin. While isolating the spleens of tumor-bearing mice, we observed a significant increase in the size of this lymphoid organ in the p38i-treated group relative to the control, suggesting active immunity upon treatment (Fig. S5F). Indeed, we found an increased frequency of IFNγ-producing splenic CD4$^+$ T cells upon p38i treatment, from 1.7% in the control group to 4% in the treated group, leading to a ≈3-fold increase in the total number of IFNγ-producing splenic CD4$^+$ T cells (Fig. 4J). Furthermore, mass cytometry analyses of bone T cells revealed higher Tbet expression, a key transcription factor for Th1 differentiation and IFNγ expression (24), in tumor proximal (mCherry+) and bystander (mCherry-) CD4$^+$ T cells from p38i-treated mice relative to the control (Fig. S5G). While we observed an increased Th1 response upon p38i treatment *in vivo*, no direct impact of p38i in CD4$^+$ T cell differentiation or IFNγ production by Th1 CD4$^+$ T cells was observed *in vitro* (Fig. S6A, S6B, S6C). Collectively, these data show that inhibition of p38α in metastasis-bearing mice increased the activation of CD4$^+$ T cells and IFNγ secretion by CD4$^+$ T cells that contributed to limited tumor growth.

Th1 lymphocytes can target tumor cells through different mechanisms independent of CD8$^+$ T cells (23). Among these mechanisms, direct cytotoxic activity through engagement of tumor cell MHCII and IFNγ-mediated cytostatic effect have been shown (23). To determine whether either of these mechanisms were effective in our system, we used CRISPR-Cas9 to knock out the MHCII gene H2-Ab1 (beta subunit of C57Bl/6 murine MHCII) in PyMT-BO1 tumor cells. Two clones of H2-Ab1-deficient PyMT-BO1 cells were selected and the absence of MHCII was confirmed upon IFNγ stimulation by flow cytometry (Fig. S7A). In separate cells, we utilized the same approach to delete Ifngr1 (the ligand-binding subunit of IFNγ receptor). Ifngr1-deficiency was confirmed by assessing tumor cell proliferation in response to IFNγ. While the parental PyMT-BO1 cells showed impaired proliferation after IFNγ stimulation in a dose-dependent manner (Fig. S7B), Ifngr1-deficient PyMT-BO1 cells were insensitive to IFNγ (Fig. S7C). After confirming the lack of MHCII and IFNGR1 expression in the respective PyMT-BO1 clones, each newly generated cell line was implanted through i.c. injection into albino C57Bl/6 mice. Then, mice were randomized into p38i or vehicle treatment group. Neither the lack of MHCII or IFNGR1 on the

tumor cells reversed the antitumor effect of p38i (Fig. S7D, S7E, S7F). Accordingly, no relevant expression of MHCII in PyMT-BO1 tumor cells isolated from tumor-bearing femurs (<2% of MHCII$^+$ PyMT-BO1) was observed in control and p38i-treated groups (Fig. S7G). Together, these data indicate that p38i does not limit metastatic tumor growth by stimulating the cytotoxic activity of CD4$^+$ T cells or by direct cytostatic activity of IFNγ on PyMT-BO1 tumor cells *in vivo*.

OX40 activation synergizes with p38α inhibition to limit metastases

We have shown that p38i treatment shifts the macrophage phenotype towards a tumor-suppressive phenotype in our mouse model (Fig. 2). Concurrently, CD4$^+$ T cells produced more IFNγ, which was required to limit tumor growth in a metastatic setting upon p38i (Fig. 4). Together, these results suggested that we could leverage p38i therapy in combination with checkpoint immunotherapy to further limit breast cancer progression. To build a rationale for which immune checkpoint could render synergism in combination with p38i, we searched for the expression levels of multiple checkpoint receptors/ligands in the myeloid APC cluster shown in Fig. 2B. Although Cd274 (i.e., PD-L1) expression was detected in myeloid APCs from both vehicle and p38i groups (Fig. S8A), the combination of p38i and anti-PD1 failed to significantly decrease metastatic tumor growth in comparison to p38i as a single agent in the PyMT-BO1 model (Fig. S8B). A deeper examination of several positive costimulatory receptors/ligands genes, including Cd40, Cd80, Cd86, Tnfsf9 and Tnfsf4, in our scRNAseq dataset revealed that the expression of Tnfsf4 (i.e., OX40L) was largely undetected in myeloid APCs (Fig. 5A). Indeed, flow cytometry analyses confirmed that less than 3% of metastasis-associated (mCherry+) CD11b$^+$GR1$^-$ myeloid cells expressed OX40L, in contrast with other costimulatory molecules, such as CD86 and CD80 that were widely expressed in all conditions (Fig. S8C). Furthermore, analyses of our human scRNAseq dataset (Fig. 3E) showed that macrophages from human bone metastases similarly expressed low levels of TNFSF4 (Fig. 5B). OX40L is the ligand for OX40, which is expressed on different immune cell populations, including T cells where its engagement can promote T cell expansion and survival after TCR activation (25). Given OX40L was not detected in our mouse or human data, we rationalized that an OX40 agonist (i.e., activating antibody) in combination with p38i would stimulate a more robust T cell response and enhance the antitumor effects of p38i. To test the efficacy of OX40 activation in combination with p38i, PyMT-BO1 cells were implanted through i.c. injection and mice were treated as shown in Fig. 5C. Importantly, implanted tumor cells were detected in the hindlimbs as early as one day or two days after i.c. injection by BLI or FDG PET scan, respectively (Fig. S1H, S8D), suggesting that the initiation of treatment is relevant to the clinical scenario. While agonist anti-OX40 and p38i, as single agents, moderately reduced (3-fold reduction) metastatic tumor growth, the combination treatment synergistically limited (≈15-fold reduction) tumor growth on day 13 (Fig. 5D). Accordingly, a similar synergistic effect was observed when we assessed the tumor burden in the hindlimbs of the mice treated with p38i and anti-OX40 (Fig. S8E). The combination of p38i and anti-OX40 also significantly increased overall survival (Fig. 5E). To assess whether this combinatorial effect could be extended to other metastatic breast cancer models, EMT6 breast tumor cells were implanted through i.c. injection and mice were randomized onto treatment based on the BLI-assessed tumor burden 5 days after tumor implantation (Fig. 5F). The combination treatment induced

a 5.6-fold reduction in tumor growth on day 12 and increased overall survival in comparison to all other groups. In contrast, p38i and anti-OX40, as single agents, induced a 2.1– and 1.6– fold reduction in metastatic growth, respectively, and failed to improve overall survival (Fig. 5G, 5H). Consistently, the combinatorial approach reduced EMT6 tumor burden to a similar degree in the hindlimbs of these mice (Fig. S8F). Collectively, these data show that the combination of p38i and OX40 activation can cooperate to further limit metastatic tumor growth and improve overall survival in these highly aggressive metastatic models.

OX40 activation can enhance both CD4$^+$ and CD8$^+$ T cell responses (25). The enhanced antitumor response that we observed by combining p38i and agonist anti-OX40 led us to investigate whether T cell activation was increased in this setting. Next, we isolated femur bones of PyMT-BO1 tumor-bearing mice from each treatment group and analyzed T cells by flow cytometry. Consistent with previous results (Fig. 4H), we found ≈32% of activated (CD62L$^-$CD44$^+$) CD4$^+$ T cells in the p38i group in comparison to ≈20% of activated CD4$^+$ T cells in the control group, while CD8$^+$ T cell activation remained unaffected upon p38i treatment (Fig. 5I). As expected, agonist anti-OX40, as a single agent, induced increases in CD4$^+$ (≈63%) and CD8$^+$ (≈20%) T cell activation (Fig. 5I). Intriguingly, the combinatorial treatment greatly augmented CD8+ T cell activation (≈46%) when we assessed CD62L and CD44 activation markers (Fig. 5I), while it significantly increased the frequency of PD1$^+$cells in both T cells population (Fig. S8G). Together, these data show that the combinatorial approach of OX40 agonism and p38α inhibition can further enhance T cell activation with a greater impact on cytotoxic CD8$^+$ T cells.

OX40 activation in combination with p38α inhibition results in a durable antitumor response and the induction of immunologic memory in the presence of a CD8$^+$ T cell neoantigen

The synergistic effect of p38i and agonist anti-OX40 on CD8$^+$ T cell activation (Fig. 5I) suggested that cytotoxic T cells play a role in the antitumor response induced by this approach. Thus, to ascertain how OX40 was acting in our model, we returned to the combination treatment of p38i and anti-OX40 but also depleted CD8$^+$ T cells. Using this approach, we found that p38i plus anti-OX40 was as effective at limiting tumor growth in the presence or absence of CD8$^+$ T cells (Fig. 6A), indicating that anti-OX40 did not operate through a CD8$^+$ T cell response. This finding raised the possibility that CD8$^+$ T cells were inoperative because of a lack of a CD8$^+$ T cell antigen (CD8 neoantigen) in PyMT-BO1 breast tumor cells. To address this possibility, we modified PyMT-BO1 cells to express ovalbumin which bears a CD8 neoantigen (Fig. S9A). We implanted the newly generated PyMT-BO1-OVA cells through i.c. injection into C57Bl/6 albino mice and randomized them onto treatment. While mice in the vehicle control group developed severe disease with disseminated metastases, p38i or anti-OX40, as single agents, again significantly reduced tumor growth and extended median overall survival by 44 and 37 days, respectively (Fig. 6B, 6C). In sharp contrast, the combination of p38i and anti-OX40 completely blocked metastatic tumor growth in all tumor-implanted mice (Fig. 6B, 6C). Indeed, all mice under the combined p38i and anti-OX40 treatment developed long-term memory against the tumor, as evidenced by a rechallenge experiment. While PyMT-BO1-OVA cells implanted into the mammary fat pad of naïve mice grew robustly, implantation of PyMT-BO1-OVA cells into

mice that underwent the combination treatment failed to grow in the primary site (Fig. 6D). Together, these data imply that inhibition of p38α reprograms the tumor stroma to increase the effectiveness of agonist anti-OX40 immunotherapy in the context of antigenic metastatic breast cancer.

Tumor antigenicity and a 'p38 inactive' gene signature predicts better outcomes in human breast cancer patients

We have shown that p38i relies on innate and adaptive players to increase an IFNγ response within the metastatic bone microenvironment (Fig. 2, 4, S2). IFNγ-responsive factors (e.g., H2-Aa, H2-Ab1, Cxcl9, B2m) were present in the upregulated macrophage gene signature upon p38α inhibition (up in p38i, Fig. 2D), that we refer to as 'p38 inactive' gene signature. Next, we sought to determine whether this 'p38 inactive' gene signature (Fig. 2D, S9B, S9C) was relevant in the human setting. Once again, we used the TCGA database to assess whether the 'p38 inactive' gene signature could predict patient outcome. Indeed, patients with breast tumors harboring high expression of the 'p38 inactive' gene signature showed better overall survival in comparison to patients with tumors harboring low expression when all subtypes were grouped together (Fig. 6E). When examining individual subtypes of human breast cancer, we found that Her2+ breast cancer patients with high expression of this signature also showed significantly better outcomes (Fig. 6E). In addition, while failing to reach statistical significance, a trend in better overall survival also existed in patients with high expression of the 'p38 inactive' signature from other subtype groups, such as luminal A and B (Fig. 6E). TCGA database does not discriminate between stroma and tumor areas, hence we sought to determine whether the same predictive value for the 'p38 inactive' signature was observed when using a stroma-specific dataset of human breast cancer samples (GSE9014(20)). Accordingly, patients with tumor-associated stroma harboring high expression of 'p38 inactive' gene signature showed better overall survival in comparison to those with low expression (Fig. S9D). Together, these data show that the 'p38 inactive' gene signature can predict better outcome for a subset of patients with breast cancer.

We have shown that the therapeutic response to p38i was enhanced in the presence of a CD8 neoantigen in our mouse model (Fig. 6B, 6C). Tumor mutational load has been associated with neoantigenicity and better immunotherapy responses in other cancer types (26, 27). Therefore, we asked whether tumor antigenicity in combination with the 'p38 inactive' gene signature was associated with better clinical outcome in human patients. To assess this hypothesis, human breast tumors from the TCGA database were classified according to their tumor mutation burden as a surrogate for neoantigenicity. In this setting, we found that a higher expression of the 'p38 inactive' gene signature was associated with better outcomes when analyzing all breast cancer patients and luminal B patients with high tumor mutational burden (high TMB) (Fig. 6F). When analyzing patients for the risk (hazard ratio) of death, the 'p38 inactive' signature was associated with a reduced risk (HR=0.406; p=0.00158) among breast cancer patients with high TMB in comparison to all breast cancer patients (HR=0.744; p=0.00983) (Fig. 6G, S9E). Accordingly, we also observed a reduced risk of death among patients with tumor stroma harboring high 'p38 inactive' signature expression (HR=0.145; p=0.0234) (Fig. S9F). Collectively, these data show that the 'p38 inactive'

macrophage gene signature correlates with reduced risk of death in all breast cancer patients and those with high TMB show an even lower risk.

Our findings showed that p38i shifts macrophage phenotype from an immunosuppressive phenotype (M2-like) towards a tumor suppressive phenotype (M1-like) in metastasis-bearing mice (Fig. 2). In addition, we found that CD4$^+$ T cells are required to limit metastatic growth upon p38i treatment (Fig. 4). Next, we sought to determine whether the 'p38 inactive' gene signature is associated with the presence of CD4$^+$ T cells and M1-like macrophages in human breast tumors. To test this hypothesis, high and low 'p38 inactive' TCGA samples (Fig. S9C) were submitted to digital cytometry analyses and CD4$^+$ T cell, M1-like and M2-like macrophages abundances were assessed. In accordance with our mouse models, high 'p38 inactive' gene signature correlated with lower abundance of M2-like macrophages and higher abundance of CD4$^+$ T cells and M1-like macrophages (Fig. 6H). Together, these data suggest that blocking the p38α pathway would limit M2-like macrophage and increase CD4$^+$ T cell/M1-like macrophage infiltration in human breast tumors.

Discussion

The importance of the tumor stroma is well established during cancer progression from early primary lesions to advanced metastases. However, the mechanisms by which the TME components contribute to cancer growth are not fully understood, especially in the metastatic setting. Here, we showed that p38MAPKα (p38α) deletion in hematopoietic cells reduced metastatic tumor growth in multiple tissues, including the bone (Fig. 1). These findings are consistent with our previously published data that p38α knockdown in breast tumor cells does not affect their metastatic potential (12). Our findings further showed that p38α inhibition limited Arg1 expression in BMMs upon alternative activation (M2) while it had no direct impact in M1 phenotype (Fig. 3), in accordance with previously published studies showing a role for the p38MAPK (p38) pathway in M2-like macrophage polarization in vivo and in vitro (10, 16). In addition, p38i shifted metastasis-associated macrophages from a tumor-promoting phenotype to a tumor-suppressive phenotype in vivo (Fig. 2). p38i also increased CD4$^+$ T cell activation and IFNγ production, which were required for the antitumor effects of p38i in our model (Fig. 4). Finally, we found that a p38-dependent gene signature from metastasis-associated macrophages was present in myeloid cells from human breast metastases in the bone (Fig. 3). Collectively, these data show that hematopoietic stromal p38α signaling is required to drive tumor-associated macrophages towards an immunosuppressive phenotype that limits adaptive T cell immune responses.

Our findings suggest an important role for p38α in tumor-associated macrophages in the context of breast cancer metastases. However, we cannot rule out that blocking p38α signaling in other immune cell populations also contributes to the p38i-mediated antitumor effects. p38 signaling plays important roles in T cell physiology. Non canonical activation of p38α and p38β can drive intra-tumoral CD4$^+$ T cells to produce TNFα and IL10 in a pancreatic cancer mouse model (15). More recently, Gurusamy and colleagues showed that p38α deletion or pharmacological inhibition enhances ex vivo expansion of tumor-infiltrating CD8$^+$ T cells (TILs) with an increased memory phenotype (28). The same study also showed that pharmacological p38 inhibition increased IFNγ production and

cytotoxicity of CD19-specific CAR CD8$^+$ T cells (28). In contrast to these reports, CD8$^+$ T cells do not contribute to the antitumor effects of p38i in our PyMT-BO1 model (Fig. 4) and we did not observe any direct impact of p38i on CD4$^+$ T cell differentiation or on IFNγ production by Th1 CD4$^+$ T cells *in vitro* (Fig. S6). Together these findings argue that p38i does not directly impact T cells in our model. Finally, p38MAPK inhibition can increase OX40L expression in bone marrow-derived dendritic cells (DCs), which directly impacts CD4$^+$ T cell activation in vitro by suppressing regulatory CD4$^+$ T cells (14). However, in our murine scRNAseq analyses (Fig 5A), we found that OX40L (i.e. Tnfsf4) is poorly expressed in myeloid APCs (Fig. 5A), and in tumor proximal (mCherry+) CD11b$^+$GR1$^-$ myeloid cells (Fig. S8C) that includes conventional DCs type 2, suggesting that OX40L regulation by p38 signaling does not play a role in our model.

CD4$^+$ T cells can directly contribute to antitumor immunity (19, 29–31). Indeed, cytotoxic CD4$^+$ T cells have been described in multiple cancer mouse models and in human cancers, including breast cancer (29). An unbiased study of the immune compartment in human breast tumors revealed the presence of cytotoxic CD4$^+$ T cells expressing cytolytic effector genes, such as GZMA and GZMK (30). Another study showed that tumor-reactive CD4$^+$ T cells require direct TCR engagement by MHCII-expressing tumor cells to develop cytotoxic activity (32). However, we found that while the PyMT-BO1 cells express MHCII in response IFNγ stimulation, MHCII-deficient clones that we created were responsive to p38i treatment after i.c. implantation (Fig. S7A, S7D, S7E), arguing against a role for cytotoxic CD4$^+$ T cells in our model. In addition to their putative cytotoxic role, CD4$^+$ T cells can limit tumor progression by secreting IFNγ to directly limit tumor cell growth or induce death (19, 33). We ruled out a direct role for IFNγ in our model by removing the Ifngr1 gene from PyMT-BO1 cells and showing these cells remained sensitive to the antitumor effects of p38i in vivo (Fig. S7B, S7C, S7F). Together, these data show that CD4$^+$ T cells do not directly target tumor cells to restrain metastatic growth after p38i treatment. However, we did find that metastasis-associated macrophages upon LPS + IFNγ stimulation killed PyMT-BO1 cells (Fig. S3A, S3B), suggesting that IFNγ-producing CD4$^+$ T cells drive macrophage-mediated killing in response to p38i in the metastatic setting.

Immune checkpoint therapy (ICT) has remarkably changed the fate of melanoma patients (34). However, the full benefits of immunotherapy have yet to come to many other patients with solid tumors, including breast cancer patients. To date, only a small fraction of PD-L1+ triple negative breast cancer (TNBC) patients benefit from anti-PD1 ICT (35). While there are likely many reasons why most breast cancer patients do not benefit from current cancer immunotherapy, a common reason is the fact that breast tumors are typically considered "cold" (not-inflamed). Substantial effort has been placed on approaches to turn cold tumors into "hot" (inflamed) tumors. Among these approaches, targeting the innate immune compartment is a relevant strategy to increase the response to current ICT. Here, we showed that targeting stromal p38α signaling limits M2-like macrophage polarization *in vitro* and *in vivo* (Fig. 2, 3). Concurrently, we showed that metastasis-associated myeloid cells poorly express OX40L in mouse and human bone metastases, making agonist anti-OX40 an ideal candidate for a combination therapy with p38i. Indeed, combination of p38i and anti-OX40 led to synergistic reduction in tumor growth and increased overall survival in two different metastatic breast cancer mouse models (Fig. 5). Currently, three different agonist anti-OX40

antibodies are in phase II clinical trials in cancer (34), including breast cancer, and other p38 inhibitors have been well tolerated in clinical trials for non-cancer indications (8). Therefore, given the p38 signature we uncovered in patient tumors, combinatorial treatment with p38i and agonist anti-OX40 is an attractive approach to improve current metastatic breast cancer therapy.

The synergistic cooperation between p38i and anti-OX40 occurred in the absence of CD8$^+$ T cells (Fig. 6A), suggesting a lack of CD8 neoantigens in the PyMT-BO1 model, which is reminiscent of the lack of neoantigens in many human cancers (36). Because CD8+ T cells are the most potent effectors of ICT response (37), we asked if the presence of a CD8 neoantigen could increase the efficacy of our combinatorial approach. This led to the surprising finding that the combination of p38i, anti-OX40 and a CD8 neoantigen resulted in a curative response in all treated mice (Fig. 6B, 6C) that we have failed to obtain in our models with classic chemotherapy approaches (12). Critically, this antitumor response was coincident with durable immunologic memory (Fig. 6D). This finding led us to seek human correlatives for increased p38i response in breast cancer patients with a high tumor mutational burden (TMB) as a surrogate for neoantigenicity (27). Using TCGA data, we found that breast cancer patients with high TMB and a high 'p38 inactive' signature score had significantly increased overall survival compared to patients with a low 'p38 inactive' signature score (Fig. 6). Furthermore, a higher 'p38 inactive' gene signature score was significantly associated with reduced risk of death among all breast cancer patients, and this risk was even lower when we analyzed only high TMB patients (Fig. 6). Together, these findings suggest that patients with a high TMB would benefit the most from the p38i + anti-OX40 approach. For those patients with a low TMB, our findings suggest that increasing the TMB via chemotherapy or radiotherapy (38, 39) could drastically increase the efficacy of a p38i+anti-OX40 approach. Collectively, our work demonstrates that a detailed analysis of the metastatic TME can identify novel therapeutic combinations that may have a significant impact on breast cancer patients.

Materials and Methods

Animals

Female B6(Cg)-Tyr^{c-2J}/J (B6 albino, The Jackson Laboratory - JAX, #000058) mice (age 6–8 weeks) were used in all experiments involving PyMT-BO1 and EO771 cell injections, unless stated otherwise. Albino C57Bl/6J mice were used to increase sensitivity of bioluminescence detection. Female FVB/N (JAX, #001800) mice (age 6–8 weeks) were used in all experiments involving NT2.5 cell injections. Female BALB/c (JAX, #000651) mice (age 6–8 weeks) were used in all experiments involving EMT6 cell injections. B6.129S4-$Arg1^{tm1.1Lky}$/J (YARG) mice were obtained through a collaboration with Dr. Katherine Weilbaecher. B6.129S2-$Tcra^{tm1Mom}$/J (Tcra–/–, #002116), B6.129S2-$H2^{dlAb1-Ea}$/J (MHCII-/-, #003584) and B6.129S2-$Ighm^{tm1Cgn}$/J (mutMt-, #002288) mouse strains were obtained from JAX. B6.SJL-$Ptprc^a$ $Pepc^b$/BoyJ (CD45.1 B6, #002014) mice (age 6–8 weeks) were also obtained from JAX and used as recipients for bone marrow transplantation experiments. p38α$^{fl/fl}$ ($Mapk14^{fl/fl}$) mice on C57Bl/6NJ strain background (40) were a kind gift from Dr. Tatiana Efimova. B6.Cg-

$Gt(ROSA)26Sor^{tm14(CAG-tdTomato)Hze}$/J (Ai14 – Cre-reporter mouse strain) and B6.Cg-$Ndor1^{Tg(UBC-cre/ERT2)1Ejb}$/1J (UBC-CreERT2 – tamoxifen-inducible Cre-expressing mouse strain) mice were a kind gift from Dr. Marco Colonna. UBC-CreERT2 mice express tamoxifen-responsive Cre recombinase under the regulation of the human ubiquitin C (UBC) promoter (constitutive). Ai14 strain is a Cre reporter strain that contains a LoxP-STOP-LoxP (LSL) cassette blocking the expression of tdTomato reporter gene in the absence of Cre activity. $Mapk14^{fl/fl}$, UBC-CreERT2 and Ai14 strains were interbred to generate UBC-CreERT2$^{Tg/0}$ $Mapk14^{fl/fl}$ Ai14$^{LSL/LSL}$ (Cre+) and $Mapk14^{fl/fl}$ Ai14$^{LSL/LSL}$ (Cre-) mice. The resulting Cre+ and Cre- littermates were on a mixed C57Bl/6J (70–75%);C57Bl/6NJ (20–25%) genetic background according to the SNP panel analysis performed by Transnetyx (Cordova, TN). All other C57Bl/6 transgenic strains were on C57Bl/6J background, unless stated otherwise. Aged female mice were obtained from the NIA aging colony. Female mice were used for all experiments described in the present work. All mice were housed and all animal procedures were approved by Washington University's Institutional Animal Care and Use Committee (IACUC).

Tumor cell implantation and survival follow-up

For intracardiac (i.c) tumor cell implantation, the designated tumor cells (PyMT-BO1, $5x10^4$; EO771, 10^5; EMT6, $2.5x10^4$; NT2.5, 10^5) were resuspended in 50μl of PBS and injected into the left ventricle of the heart of mice under anesthesia with 5μl/g of ketamine/xylazine cocktail (17.7g/ml of ketamine and 2.65mg/ml of xylazine). For spontaneous metastasis and PyMT-BO1-OVA rechallenge experiments, the designated tumor cells admixed in matrigel were implanted into the mammary gland after a small incision to expose the 4th inguinal mammary fat pad of mice under anesthesia with 5μl/g of ketamine/xylazine cocktail. For survival follow-up, death events were counted when mice were found dead, had both hindlimbs paralyzed, had a tumor larger than 2cm or showed >20% of weight loss for 2 consecutive days, whichever happened first.

Oral dosage of p38MAPKα inhibitor

The p38MAPKα small molecule inhibitor CDD-111 (13) (Aclaris Therapeutics, St. Louis, MO) was compounded at 700ppm with Purina Rodent Chow #5001 (Research Diets Inc., New Brunswick, NJ), rendering 0.7g of CDD-111 per kg of chow. Mice were fed *ad libitum*, resulting in a median plasma concentration of 356ng/ml (178–521ng/ml – 25th-75th percentiles).

Cell culture

PyMT-BO1 mouse breast carcinoma cells were obtained through collaboration with Dr. Katherine Weilbaecher's laboratory (41). EO771 and EMT6 mouse breast carcinoma cells were obtained from ATCC (#CRL-3461 and #CRL-2755, respectively, ATCC, Manassas, VA). The NT2.5 HER2/neu+ mouse breast carcinoma was a kind gift from Dr. Elizabeth Jaffee. All cell lines but NT2.5 were cultured in DMEM supplemented with 10% heat-inactivated FBS (#F2442, Sigma, St. Louis, MO) and antibiotics (100U/ml of Penicillin and 100 μg/ml of Streptomycin, #P0781, Sigma, St. Louis, MO). The NT2.5 cell line was cultured in RPMI supplemented with 20% heat-inactivated FBS, 1.2% HEPES, 1% L-glutamine, 1% non-essential amino acids, 1% sodium pyruvate, 0.2% insulin, 0.2%

gentamycin and antibiotics. All cell lines were used at low-passage and regularly tested for Mycoplasma by PCR. Primary cultures of splenocytes and lymph node-extracted lymphocytes were maintained in RPMI supplemented with 10% heat-inactivated FBS, 1mM sodium pyruvate, 55nM 2-mercaptoethanol, 10mM HEPES, 1X MEM non-essential amino acids (#25-025-CI, Corning, Corning, NY),1X GlutaMAX (#35050-061, Gibco, Waltham, MA) and antibiotics.

Plasmid construction and lentiviral transduction

Ifngr1- and H2-Ab1-deficient PyMT-BO1 clones were generated by CRISPR using a combination of two gDNAs per gene as follows: Ifngr1-1 5' ATGGGCCCGCAGGCGGCAGC 3'; Ifngr1-2 5' TGGAGCTTTGACGAGCACTG 3; H2-Ab1-1 5' CATTACCTGTGCCTTAGAGA 3'; H2-Ab1-2 5' TGATGGTGCTGAGCAGCCCA 3'. The above gDNAs were cloned into LentiCRISPRv2 Hygro and LentiGuide-Puro plasmids. LentiCRISPRv2 Hygro plasmid was a kind gift from Dr. Brett Stringer (Addgene plasmid #98291). LentiGuide-Puro plasmid was a kind gift from Dr. Feng Zhang (Addgene plasmid #52963). PyMT-BO1-sLPmCher and PyMT-BO1-OVA cell lines were generated by lentiviral transduction using pRRL-sLPmCherry and pLenti-OVA-P2A-Puro vectors, respectively. The pRRL-sLPmCherry plasmid was a kind gift from Dr. Ilaria Malanchi (18). pLenti-OVA-P2A-Puro was generated by cloning the full length OVA cDNA into Cas9-excised pLenti-Cas9-P2A-Puro by Gibson assembly. The pLenti-Cas9-P2A-Puro plasmid was a kind gift from Dr. Lukas Dow (Addgene plasmid #110837). HEK293T cells were transiently transfected with lentiviral accessory plasmids (VSV.G and psPAX2) and the designated transfer plasmid using TransIT-293 transfection reagent according to the manufacturer instructions (#MIR2700, Mirus Bio LLC, Madison, WI). The virus containing cell supernatant was collected and .45μm-filtered after 48h from transfection, supplemented with 8 mg/ml protamine sulfate and immediately used for transduction of target cells. After infection, target cells were FACS sorted or selected accordingly to the respective reporter gene. For all generated cell lines, transgene expression or CRISPR target knockout was confirmed by flow cytometry or western blot, with the exception of the Ifngr1 KO cell line that was confirmed by assessing tumor cell responsiveness upon stimulation with IFNγ.

Neutralizing/Blocking and Agonist Antibodies

To deplete T cells, CD4- and/or CD8-neutralizing (anti-CD4, Clone: GK1.5; anti-CD8, Clone: 2.43) IgG antibodies were administered via i.p. injections into mice 2 days prior to tumor cell implantation using the following regime: 1st injection containing 500mg and subsequent injections containing 250μg (every 4 days) of each antibody. To deplete/block NK cells or IFNγ, the same dosage was administered similarly using the respective neutralizing/blocking antibodies (anti-NK1.1, Clone: PK136; anti-IFNγ, Clone: XMG1.2). Effective depletion of NK and T cells was routinely assessed by flow cytometry of peripheral blood. To deplete macrophages, CSF1-blocking IgG antibody (anti-CSF1, Clone: 5A1) and clodronate liposomes (Liposoma, Netherlands) were administered according to the following regime: 1st injection of anti-CSF1 containing 1mg was administered via i.p. injection into mice 3 days prior tumor cell implantation and subsequent injections containing 500μg were administered every 4 days; 1st injection of clodronate liposomes containing

200μl was administered via i.p. injection into mice 2 days prior tumor cell implantation and subsequent injections of the same volume were administered every 4 days. For the immunotherapy regimen, 200μg of agonist OX40 (anti-OX40, Clone: OX-86) or 200μg of blocking PD-1 (anti-PD-1, Clone: RMP1-14) IgG antibody was administered via i.p injection starting 1 day or 5 days (as indicated) after tumor cell implantation every 4 days for a total of 3 doses. All neutralizing/blocking and agonist antibodies were purchased from BioXcell (Lebanon, NH).

Bioluminescence Imaging (BLI)

BLI was performed as previously described (42). In vivo imaging was performed on an IVIS50 or IVIS Lumina (PerkinElmer, Downers Grove, IL; Living Image 3.2, 1–60sec exposures, binning 4, 8 or, 16, FOV 15cm, f/stop1, open filter). Mice were injected intraperitoneally with D-luciferin (150mg/kg in PBS; Gold Biotechnology) and imaged 10 minutes later under isoflurane anesthesia (2% vaporized in O2). For ex vivo imaging, animals were sacrificed immediately following whole body imaging and both hind limbs and organs were isolated and imaged for 10 seconds. For analysis, total photon flux (photons/sec) was measured from a fixed region of interest (ROIs) over the whole body, hindlimbs or bones using Living Image 2.6 software. For all experiments using intracardiac injections, disseminated metastatic tumor burden was assessed on day 12/13/14 after tumor cell implantation as indicated in figure legends, with the exception of the experiment using PyMT-BO1-OVA cell line where metastatic tumor burden was assessed dynamically by weekly BLI. For live imaging, data was plotted as fold-change relative to day 1/2 after tumor cell implantation when available.

Western Blot

Total protein from tumor cells or bone marrow pellets was obtained from lysis in 1X RIPA buffer (#20-188, Sigma) containing 1X protease inhibitor cocktail (#P8340, Sigma), 1X phosphatase inhibitor cocktail (#524624, Sigma) and 1mM PMSF (#52332, Sigma) followed by sonication on ice and incubation at 100°C for 10 min. Total cell lysates were resolved by SDS-PAGE, and the separated proteins were transferred onto a nitrocellulose membrane. The antibodies used were as follows: GAPDH monoclonal antibody (#G8795, Sigma), β-tubulin polyclonal antibody (#ab6046, Abcam, Waltham, MA), p38α polyclonal antibody (#9218, Cell Signaling Technology, Danvers, MA), arginase-1 monoclonal antibody (#93668, Cell Signaling Technology), phospho-MK2 polyclonal antibody (#3041, Cell Signaling Technology), MK2 polyclonal antibody (#3042, Cell Signaling Technology) and Ovalbumin polyclonal antibody (#PA1-196, ThermoFisher Scientific, Waltham, MA). Immunodetection was performed with Pierce ECL Western Blotting Substrate (#32106, ThermoFisher Scientific, Waltham, MA).

Bone marrow transplantation

Recipient C57BL/6 CD45.1 mice received two doses of 400 cGy four hours apart, followed by transplant of bone marrow by retro-orbital injection (i.v.). Irradiation was carried out using an X-ray irradiator (XRAD 320). Donor bone marrow was prepared as follows: donor mice were sacrificed by CO_2 inhalation, both femurs, tibias and ilia were extracted in a sterile setting and flushed using pulsed centrifugation to collect marrow. Bone marrow was

reconstituted in cold sterile serum-free 1X HBSS and injected i.v. at a concentration of 5 million cells per 200μL per mouse. Mice were monitored over 2 weeks for signs of radiation sickness or weight-loss. 6-week post irradiation, mice were given 500mg/kg tamoxifen-compounded chow (#TD.130858, Envigo, St. Louis, MO) for one week (equivalent to 80mg/kg daily dosage according to the manufacturer), followed by another week of washout period. At last, tumor cells were implanted as indicated.

Immunohistochemical staining

Bones were fixed in 10% neutral buffered formalin for 18 hours, followed by decalcification for 2 weeks in 14% EDTA solution, dehydrated in graded-ethanol, embedded in paraffin and sectioned into 5μm sections using a microtome. For frozen sections, bones were fixed in 4% PFA solution for 18 hours, followed by decalcification for 3 days in 14% EDTA solution and 30% sucrose gradient, embedded in OCT and sectioned into 10μm sections using a cryostat. Automated staining of tissues was carried out on the Bond Rxm (Leica Biosystems) following dewaxing when applicable and appropriate epitope retrieval. Immunostaining was chromogenically visualized using the Bond Polymer Refine Detection alone (#DS9800 or # DS9390, Leica Biosystems) or in conjunction with Bond Intense R Detection Systems (#DS9263, Leica Biosystems). Antibodies are listed in Supplementary Table 1. Slides were mounted using Xylene-based Cytoseal (ThermoFisher) or Vectamount (Vector Labs) as appropriate. Next, slide images were obtained at a Zeiss AxioScan 7 microscope. All immunohistochemical analyses were performed on the HALO image analysis platform (Indica Labs, Albuquerque, NM).

Murine sample preparation for flow cytometry, mass cytometry and scRNAseq

Femur bones were crushed using a pestle and a mortar and digested with collagenase (2mg/ml) for 45min at 37°C with agitation. For tumor-bearing femurs, the central diaphysis area was discarded since this region often shows no tumor lesions. After digestion, the cell suspension was filtered through a 70μm cell strainer. Then, the samples underwent red blood cell lysis on ice for 5min. Blood samples underwent red blood cell lysis at room temperature for 10 min. Splenocytes were mechanically extracted by mashing the spleen on a 70μm strainer and collected in a 50ml conical centrifuge tube followed by red blood cell lysis on ice for 5min. Hereafter, sample handling was entirely carried out on ice unless stated otherwise.

Human sample collection and processing

Histological patient samples were obtained in accordance with recognized ethical guidelines, approved by the Washington University's Institutional Review Board (IRB #201102394; waiver of consent under the same IRB#) with Waiver of Elements of Consent as per 45 CFR 46.116 (d). All patient information was deidentified prior to investigator use. All of the human research activities and all activities of the IRBs designated in the Washington University Federal Wide Assurance, regardless of sponsorship, are guided by the ethical principles in "The Belmont Report: Ethical Principles and Guidelines for the Protection of Human Subjects Research of the National Commission for the Protection of Human Subjects of Biomedical and Behavioral Research". All metastatic samples displayed tumor

cells, as determined by analysis of serial sections stained for pan-cytokeratin along with either p-p38 or p-MK2.

Four freshly dissected bone metastases (BoM) were collected during surgery from 3 patients with estrogen receptor positive primary breast cancer via the Pitt Biospecimen Core of the University of Pittsburgh and the Tissue and Research Pathology Services of the UPMC Hillman Cancer Center. These patients had a metastatic bone lesion that caused a bone fracture and were eligible for surgery to repair the broken bone. All samples were collected with written informed consent and approval from the Institutional Review Board (IRB) at the University of Pittsburgh (STUDY20010034, University of Pittsburgh) in accordance with recognized ethical guidelines. Fresh BoMs were dissociated into single cells following 10x Genomics tumor dissociation protocol (Version: RevB). Briefly, 0.2–1g tumor tissue was minced in serum free DMEM media and further dissociated by a combination of mechanical force and enzymatic digestion using Miltenyi tumor dissociation system (Miltenyi: 130-093-235, 130-095-929) according to the manufacturer's protocol. After dissociation, cell suspensions and remaining tissue were separated by filtering through 70μM strainers (Fisher: 08-771-2). Viability of dissociated cells was measured by trypan blue staining and dead cell removal was performed with dead cell removal kit (Miltenyi: 130-090-101) according to the manufacturer's protocol.

Human scRNAseq library preparation and data analysis

Freshly dissociated single cells of BoM with >= 70% viability were processed for scRNAseq library preparation following 10X genomics V3 chemistry 3' end protocol. 8,000 cells were targeted per sample. scRNA libraries were sequenced with Novaseq6000 at 70,000 reads/cell with setting read1-28bp, read2-91bp, and i7 index-8bp. Raw BCL files from Novaseq6000 were converted to FASTQ files with Cellranger's (43) (Version: 3.1.0) mkfastq function. Cellranger count function was then applied for read alignment, and barcode and UMI counting with GRCh38 as reference. scCB2 (44) and DoubletFinder (45) were used to predict and remove empty droplets and doublets of single cell data. Cells with number of features less 300 and more than 9000 were further filtered out based on the distribution of number of features detected per cell. Seurat (46) was used for data integration, normalization, dimension reduction and clustering. Briefly, data from 4 samples were merged together using Seurat merge function, log normalized and scaled with effect of mitochondrial gene scaled out. The top 3000 most variable genes across cells selected by the 'vst' method and top 15 principal components were used for clustering analysis based on louvain algorithm as they captured the majority of the variety of the data. Expression of canonical cell markers from PanglaoDB (47) and Zhang Y et al (48) and an automatic cell type assignment method SingleR (49) with Blueprint Encode reference were used to assign cell types. All gene expression shown is log normalized counts unless stated otherwise. The p38-dependent gene signature score was calculated using Seurat AddModuleScore function with default settings. Wilcoxon test was used to calculate p value comparing macrophages with other cell types.

Multiparametric flow cytometry

Following sample preparation, single cell suspensions were resuspended in flow cytometry buffer (PBS containing 1% BSA and 5mM EDTA), FcR blocked with rat anti-mouse CD16/CD32 antibodies (eBioscience) for 10 min and pelleted by centrifugation. When used, Live/Dead viability dyes and Calcein-AM-Blue were applied for 30 min at room temperature. Next, cells were labeled with 100μl of fluorophore-conjugated anti-mouse extracellular antibodies at recommended dilutions for 30 min on ice. Intracellular staining for cytokines was conducted using BD Biosciences Fixation/Permeabilization Solution Kit with BD Golgiplug, according to the manufacturer's instructions. Intracellular staining for transcription factors and other intracellular markers was conducted subsequently using the eBioscience Transcription Factor Staining buffer set, according to the manufacturer's instructions. All antibodies are listed in Supplementary Table 1. FCS Data were acquired on BD FACSCanto and BD Fortessa X-20 (BD Biosciences) and analyzed using FlowJo software (v10) with application of bead-based compensation. For live analysis of sLP-mCherry uptake, the fixation step was not performed, and labeled cells were analyzed immediately (within 2 hours) on the cytometer. For experiments that measured T cell cytokines involving ex vivo stimulation, primary cell suspensions were incubated in a 48-well plate with 1X BD Golgiplug and 1X Cell Activation Cocktail (#423302, Biolegend, San Diego, CA) for 5 hours at 37° C and 5% CO_2. After incubation, cells were resuspended in Fc block buffer and then labeled with fluorophore-conjugated anti-mouse antibodies as above. Gating strategies for macrophage and T cell flow cytometry analyses are shown in Fig. S10A and S10B.

Mass Cytometry

Femur extremities from mice (6 animals per group) bearing sLPmCherry-expressing tumors were harvested, and submitted to sample preparation. Prior to mass cytometry run, single cell suspensions were stained with anti-CD45 and Live/Dead viability dye. Then, CD45$^+$mCherry$^-$ and CD45$^+$mCherry$^+$ cell populations were sorted from each sample using a Sony iCyt Synergy SY3200 BSC cell sorter. Following sample sorting, single cell suspensions were resuspended in CyPBS (#MB-008, Rockland, Philadelphia, PA) and cisplatin viability staining was performed for 1 minute on ice and immediately quenched by adding mass cytometry buffer (CyPBS containing 0.1% BSA and 2mM EDTA). FcR blocked with rat anti-mouse CD16/CD32 antibodies (eBioscience) for 10 min and pelleted by centrifugation. Cells were then labeled with 100μl of metal isotope-conjugated anti-mouse extracellular antibodies at recommended dilutions for 30 min on ice. Intracellular staining for transcription factors and other intracellular markers was conducted subsequently using the eBioscience Transcription Factor Staining buffer set, according to the manufacturer's instructions. Next, samples were barcoded using Cell-ID 20-Plex Pd Barcoding Kit (#201060, Fluidigm, San Francisco, CA), according to manufacturer's instructions. Finally, samples were stained with Cell-ID Intercalator-Ir (#201192A, Fluidigm). Data were acquired on a CyTOF2/Helios mass cytometer, debarcoded using MATLAB-based Single Cell Debarcoder and analyzed using Cytobank software. All antibodies are listed in Supplementary Table 1. Gating strategies for mass cytometry analyses are shown in Fig. S10C.

Mouse scRNAseq and data analysis

Femur extremities from vehicle- and p38i-treated mice (4 animals per group) were harvested, washed and made into single cell suspension by digestion with collagenase. Using sLPmCherry-expressing tumor cells to label the surrounding niche, mCherry+ and mCherry- immune (CD45+) and non-immune stromal (CD45-) cells were sorted using a Sony iCyt Synergy SY3200 BSC cell sorter. Tumor cells were discarded by the exclusion of GFP+ cells. After sorting, 30,000–70,000 live cells were delivered for library construction using 10X Genomics Chromium 3′ GEM Single Cell Library v3 kit (10X Genomics, Pleasanton, CA). Sequencing was performed according to a standard pipeline at The Genome Technology Access Center at Washington University, St. Louis. The Cell Ranger Software Suite from 10X Genomics was used for sample demultiplexing, barcode processing and single-cell counting. The Cell Ranger count was used to align samples to the reference genome GRCm38 (mm10). For data analysis, the filtered feature barcode matrices were loaded into Partek Flow (St. Louis, MO). For each sample, cells that expressed less than 200 or more than 8,000 genes were excluded. Cells with greater than 10% mitochondrial RNA content, less than 1,500 counts or more than 80,000 counts were also excluded. Normalization and scaling were performed following the recommended parameters by Partek Flow. Principle component exploratory analysis (PCA) was performed to reduce dimensionality prior to clustering. Graph-based clustering was performed to improve UMAP dimensional reduction. Then, UMAP was performed on the scaled matrix using the first 20 PCA components to obtain a two-dimensional representation of the cell states. Then, the innate myeloid clusters were classified based on high expression of known marker genes for each cell population. Bone non-immune stromal cell clusters were classified based on parameters described by Baccin et al, 2020 (50). Differently expressed genes (DEGs) between two groups were calculated for each dataset. Then the DEG list from each dataset was filtered with P value <0.05 and 1.5 fold-change in any direction. These gene sets were fed into Gene Set Enrichment Analysis (GSEA) to test for KEGG pathways, Reactome and Hallmarks gene sets.

Micro-computed tomography (mCT) scanning and bone histomorphometric analysis

For *in vivo* assessment of trabecular bone mass, we used a high speed μCT system (Scanco viva CT 40) with Xray energy 70 KVp, 114 μA, and 10 μm resolution. First, mice were anesthetized using isoflurane (2.5%) and placed in the sample holder to measure the trabecular bone volume of the right femur. To maintain the anesthesia while scanning, the mice were exposed to a continuous supply of isoflurane and were occasionally monitored for breathing for 30 minutes to allow us to scan 425 slices. For the trabecular compartment, contours were traced on the inside of the cortical shell using 2D images of the femoral metaphysis. The end of the growth plate region was used as a landmark to establish a consistent location for starting analysis, and the next 100 slices were analyzed. The following trabecular bone parameters were reported: bone volume to trabecular volume fraction (BV/TV), trabecular number (Tb.N), trabecular thickness (Tb.Th), and trabecular spacing (Tb.Sp).

Generation of bone-marrow derived macrophages and macrophage polarization

Bone marrow-derived macrophages (BMM) were generated by culturing mouse bone marrow for 6 days in αMEM media supplemented with 10% heat-inactivated FBS, antibiotics (100U/ml of Penicillin and 100 μg/ml of Streptomycin) and 10% CMG media as a source of CSF1(51). For polarization assays, BMMs were culture in regular culture media without CMG supplementation in the presence of 0.25U/ml of murine IFNγ or 20ng/ml of murine IL4 and IL13 for M1 or M2 macrophage differentiation for 24h or 48h, respectively. When indicated, BMMs were pretreated with p38i two hours prior the addition of polarizing cytokines.

Macrophage-mediated killing assay

Tumor-associated (mCherry+) macrophages (TAMs) were sorted from the bone of mice that were previously i.c. injected with PyMT-BO1-sLPmCher tumor cells. TAMs/BMMs were seeded to a black 384-well clear bottom plate (Corning) for two hours. After two hours, ZsGreen labeled-PyMT-BO1 cells were seeded on the plate in ratio of 1 tumor cell to 3 TAMs/BMMs. Two hours later, 100ng/ml of LPS (Invitrogen, Waltham, MA), 33ng/ml of mouse IFNγ (Invitrogen) and p38i (2μM) were added to the medium (time point: 0 hours) alone and in combination, and live cell imaging was performed in a Cytation5 Cell Imaging Multi-Mode Reader (BioTek, Santa Clara, CA) for 48hours. Imaging was taken in 4 different areas and the ZsGreen+ area was analyzed every hour. ZsGreen+ area was normalized by the respective ZsGreen+ area at 0 hours for each sample.

CD4+ T cell differentiation and IFNγ production

Primary naïve CD4+ T cells were isolated by negative selection (#130-104-453; Miltenyi Biotec, Waltham, MA) from peripheral lymph node macerates (inguinal, axillary, brachial, and cervical). CD4+ T cell purity was verified by flow cytometry after isolation and always remained superior to 95%. Th1, Th2 and Treg differentiation were achieved as described before (52). IFNγ production was assessed by flow cytometry after adding 1X Cell Activation Cocktail (#423302, BioLegend) and 1X GolgiPlug (BD Biosciences) to *in vitro* differentiated Th1 T cell or isolated splenocyte cultures.

FDG PET scan

$[^{18}F]$FDG was produced with an average specific activity $0.3–1.1x10^{10}$ mCi/mL by the Mallinckrodt Institute of Radiology's Cyclotron Facility and Nuclear Pharmacy at Washington University School of Medicine in compliance with current good manufacturing practices. Mice were anesthetized using a Plexiglas chamber flowing with 1.5–2% Isoflurane. Mice were injected with 7.4–8 MBq $[^{18}F]$FDG via tail vein and imaged for 10 min at 1 h post-injection of the radiotracer on the small animal INVEON PET/CT scanner (Siemens Medical Solutions, Knoxville, TN). Computed tomography (CT) and corresponding PET images were co-registered on Inveon Research Workplace (IRW) software (Siemens Medical Solutions, Knoxville, TN). The reconstructed PET/CT images were viewed on IRW software, which allowed trans-axial, coronal, and sagittal displays of the slices and maximum intensity projection (MIP) PET/CT images. The volumetric regions of interest (VOI) were manually drawn using CT anatomical guidelines and total amount of

[^{18}F]FDG activity was obtained. A quantitative analysis of [^{18}F]FDG activity was performed by calculating the maximum standard uptake values (SUV$_{max}$) within a VOI using the formula: SUV$_{max}$ = (VOI maximum activity [nCi/mL] × [animal weight (g)/[injected dose (nCi)]). VOI maximum activity was decay corrected to the scan start time. Injected dose was decay corrected to the imaging time, and weight was the whole animal in grams. PET/CT images were presented as maximum intensity projections (MIP) that combine all collected VOI voxels in a 2D image. All images displayed on the same scale.

TCGA data analyses

RNA-seq counts data and patient clinical information for all TCGA-BRCA primary tumor samples were obtained from the Genomic Data Commons (53). The gene expression values were TMM-normalized using edgeR (54), the logCPM value of each gene was z-normalized and signature scores for the p38-dependent, 'p38 inactive' and SDPP (20) gene signatures were calculated for each sample by taking the mean of all genes in a set for each sample.

The relationship between each signature and patient disease outcome was then examined via analysis of 10 year overall survival data. Patients were stratified into high- and low-expression signature groups using the median signature score as a cutpoint, K-M curves for these groups were plotted in R using the survminer package, and the significance of the separation between groups was assessed by log-rank test. Hazard ratio for the high versus the low group was determined by multivariate Cox regression with patient age at diagnosis as a covariate. This analysis was repeated for each breast cancer subtype.

In order to explore the relationship between tumor CD4/CD8 antigenicity and impact of the macrophage signatures on patient tumor response, we first incorporated tumor mutational burden (TMB) values from the MC3 project (55), performing survival analysis for all TCGA-BRCA patients and those in each sub-group segregated into a high mutation group (TMB > mean) and a low mutation group. Expanding on this analysis, we used CIBERSORTx (56) to perform digital cytometry on the samples, generating CD4$^+$ T cell, M1- and M2-like macrophage abundance estimates for each sample.

Statistical Analyses

All statistical analyses were carried out using Graphpad Prism software. Unpaired or paired student t test and One-way ANOVA with Tukey multicomparison test were performed as indicated in the figure legends. Numerical data are shown as mean ± SEM, unless specifically noted. Simple randomization was performed for all animal experiments with the exception of EMT6 survival experiment shown in Fig. 5, where covariate adaptive randomization was performed based on the tumor burden assessed by BLI prior to the first treatment intervention to assure a similar tumor burden distribution in each group. Log-rank (Mantel-Cox) test was used for all survival analyses. Hazard ratios (HR) were estimated from Cox proportional hazard model with 95% confidence interval and false discovery rate (FDR) adjusted p-values were calculated for multiple comparisons. p-values <0.05 were considered statistically significant for all studies.

Supplementary Material

Refer to Web version on PubMed Central for supplementary material.

Acknowledgements

Data Availability

Human and murine scRNAseq data from metastatic lesions in the bone can be found at Gene Expression Omnibus Repository (GEO) accession numbers GSE190772 and GSE210286, respectively.

References

1. Weilbaecher KN, Guise TA, McCauley LK. Cancer to bone: a fatal attraction. Nature reviews Cancer 2011;11:411–25. [PubMed: 21593787]

2. Jiao S, Subudhi SK, Aparicio A, Ge Z, Guan B, Miura Y, et al. Differences in Tumor Microenvironment Dictate T Helper Lineage Polarization and Response to Immune Checkpoint Therapy. Cell 2019;179:1177–90 e13. [PubMed: 31730856]

3. Fox GC, Su X, Davis JL, Xu Y, Kwakwa KA, Ross MH, et al. Targeted Therapy to beta3 Integrin Reduces Chemoresistance in Breast Cancer Bone Metastases. Molecular cancer therapeutics 2021;20:1183–98. [PubMed: 33785647]

4. Fane ME, Chhabra Y, Alicea GM, Maranto DA, Douglass SM, Webster MR, et al. Stromal changes in the aged lung induce an emergence from melanoma dormancy. Nature 2022;606:396–405. [PubMed: 35650435]

5. Zhu L, Narloch JL, Onkar S, Joy M, Broadwater G, Luedke C, et al. Metastatic breast cancers have reduced immune cell recruitment but harbor increased macrophages relative to their matched primary tumors. Journal for immunotherapy of cancer 2019;7:265. [PubMed: 31627744]

6. Morgillo F, Dallio M, Della Corte CM, Gravina AG, Viscardi G, Loguercio C, et al. Carcinogenesis as a Result of Multiple Inflammatory and Oxidative Hits: a Comprehensive Review from Tumor Microenvironment to Gut Microbiota. Neoplasia 2018;20:721–33. [PubMed: 29859426]

7. Faget DV, Ren Q, Stewart SA. Unmasking senescence: context-dependent effects of SASP in cancer. Nature reviews Cancer 2019;19:439–53. [PubMed: 31235879]

8. Canovas B, Nebreda AR. Diversity and versatility of p38 kinase signalling in health and disease. Nature reviews Molecular cell biology 2021;22:346–66. [PubMed: 33504982]

9. Gui J, Zahedi F, Ortiz A, Cho C, Katlinski KV, Alicea-Torres K, et al. Activation of p38alpha stress-activated protein kinase drives the formation of the pre-metastatic niche in the lungs. Nature cancer 2020;1:603–19. [PubMed: 34124690]

10. Su X, Xu Y, Fox GC, Xiang J, Kwakwa KA, Davis JL, et al. Breast cancer-derived GM-CSF regulates arginase 1 in myeloid cells to promote an immunosuppressive microenvironment. The Journal of clinical investigation 2021;131.

11. Alspach E, Flanagan KC, Luo X, Ruhland MK, Huang H, Pazolli E, et al. p38MAPK plays a crucial role in stromal-mediated tumorigenesis. Cancer discovery 2014;4:716–29. [PubMed: 24670723]

12. Murali B, Ren Q, Luo X, Faget DV, Wang C, Johnson RM, et al. Inhibition of the Stromal p38MAPK/MK2 Pathway Limits Breast Cancer Metastases and Chemotherapy-Induced Bone Loss. Cancer research 2018;78:5618–30. [PubMed: 30093561]

13. Burnette BL, Selness S, Devraj R, Jungbluth G, Kurumbail R, Stillwell L, et al. SD0006: a potent, selective and orally available inhibitor of p38 kinase. Pharmacology 2009;84:42–60. [PubMed: 19590255]

14. Lu Y, Zhang M, Wang S, Hong B, Wang Z, Li H, et al. p38 MAPK-inhibited dendritic cells induce superior antitumour immune responses and overcome regulatory T-cell-mediated immunosuppression. Nature communications 2014;5:4229.

15. Alam MS, Gaida MM, Bergmann F, Lasitschka F, Giese T, Giese NA, et al. Selective inhibition of the p38 alternative activation pathway in infiltrating T cells inhibits pancreatic cancer progression. Nature medicine 2015;21:1337–43.

16. Suarez-Lopez L, Sriram G, Kong YW, Morandell S, Merrick KA, Hernandez Y, et al. MK2 contributes to tumor progression by promoting M2 macrophage polarization and tumor angiogenesis. Proceedings of the National Academy of Sciences of the United States of America 2018;115:E4236–E44. [PubMed: 29666270]

17. Li X, Udagawa N, Itoh K, Suda K, Murase Y, Nishihara T, et al. p38 MAPK-mediated signals are required for inducing osteoclast differentiation but not for osteoclast function. Endocrinology 2002;143:3105–13. [PubMed: 12130576]

18. Ombrato L, Nolan E, Kurelac I, Mavousian A, Bridgeman VL, Heinze I, et al. Metastatic-niche labelling reveals parenchymal cells with stem features. Nature 2019;572:603–8. [PubMed: 31462798]

19. Alspach E, Lussier DM, Schreiber RD. Interferon gamma and Its Important Roles in Promoting and Inhibiting Spontaneous and Therapeutic Cancer Immunity. Cold Spring Harbor perspectives in biology 2019;11.

20. Finak G, Bertos N, Pepin F, Sadekova S, Souleimanova M, Zhao H, et al. Stromal gene expression predicts clinical outcome in breast cancer. Nature medicine 2008;14:518–27.

21. Kinker GS, Vitiello GAF, Ferreira WAS, Chaves AS, Cordeiro de Lima VC, Medina TDS. B Cell Orchestration of Anti-tumor Immune Responses: A Matter of Cell Localization

and Communication. Frontiers in cell and developmental biology 2021;9:678127. [PubMed: 34164398]

22. Harris DP, Goodrich S, Gerth AJ, Peng SL, Lund FE. Regulation of IFN-gamma production by B effector 1 cells: essential roles for T-bet and the IFN-gamma receptor. Journal of immunology 2005;174:6781–90.

23. Basu A, Ramamoorthi G, Albert G, Gallen C, Beyer A, Snyder C, et al. Differentiation and Regulation of TH Cells: A Balancing Act for Cancer Immunotherapy. Frontiers in immunology 2021;12:669474. [PubMed: 34012451]

24. Szabo SJ, Kim ST, Costa GL, Zhang X, Fathman CG, Glimcher LH. A novel transcription factor, T-bet, directs Th1 lineage commitment. Cell 2000;100:655–69. [PubMed: 10761931]

25. Croft M, So T, Duan W, Soroosh P. The significance of OX40 and OX40L to T-cell biology and immune disease. Immunological reviews 2009;229:173–91. [PubMed: 19426222]

26. Rizvi NA, Hellmann MD, Snyder A, Kvistborg P, Makarov V, Havel JJ, et al. Cancer immunology. Mutational landscape determines sensitivity to PD-1 blockade in non-small cell lung cancer. Science 2015;348:124–8. [PubMed: 25765070]

27. Van Allen EM, Miao D, Schilling B, Shukla SA, Blank C, Zimmer L, et al. Genomic correlates of response to CTLA-4 blockade in metastatic melanoma. Science 2015;350:207–11. [PubMed: 26359337]

28. Gurusamy D, Henning AN, Yamamoto TN, Yu Z, Zacharakis N, Krishna S, et al. Multi-phenotype CRISPR-Cas9 Screen Identifies p38 Kinase as a Target for Adoptive Immunotherapies. Cancer cell 2020;37:818–33 e9. [PubMed: 32516591]

29. Oh DY, Fong L. Cytotoxic CD4(+) T cells in cancer: Expanding the immune effector toolbox. Immunity 2021;54:2701–11. [PubMed: 34910940]

30. Azizi E, Carr AJ, Plitas G, Cornish AE, Konopacki C, Prabhakaran S, et al. Single-Cell Map of Diverse Immune Phenotypes in the Breast Tumor Microenvironment. Cell 2018;174:1293–308 e36. [PubMed: 29961579]

31. Cachot A, Bilous M, Liu YC, Li X, Saillard M, Cenerenti M, et al. Tumor-specific cytolytic CD4 T cells mediate immunity against human cancer. Science advances 2021;7.

32. Quezada SA, Simpson TR, Peggs KS, Merghoub T, Vider J, Fan X, et al. Tumor-reactive CD4(+) T cells develop cytotoxic activity and eradicate large established melanoma after transfer into lymphopenic hosts. The Journal of experimental medicine 2010;207:637–50. [PubMed: 20156971]

33. Dighe AS, Richards E, Old LJ, Schreiber RD. Enhanced in vivo growth and resistance to rejection of tumor cells expressing dominant negative IFN gamma receptors. Immunity 1994;1:447–56. [PubMed: 7895156]

34. Kraehenbuehl L, Weng CH, Eghbali S, Wolchok JD, Merghoub T. Enhancing immunotherapy in cancer by targeting emerging immunomodulatory pathways. Nature reviews Clinical oncology 2022;19:37–50.

35. Cortes J, Rugo HS, Cescon DW, Im SA, Yusof MM, Gallardo C, et al. Pembrolizumab plus Chemotherapy in Advanced Triple-Negative Breast Cancer. The New England journal of medicine 2022;387:217–26. [PubMed: 35857659]

36. Schumacher TN, Schreiber RD. Neoantigens in cancer immunotherapy. Science 2015;348:69–74. [PubMed: 25838375]

37. Raskov H, Orhan A, Christensen JP, Gogenur I. Cytotoxic CD8(+) T cells in cancer and cancer immunotherapy. British journal of cancer 2021;124:359–67. [PubMed: 32929195]

38. Lussier DM, Alspach E, Ward JP, Miceli AP, Runci D, White JM, et al. Radiation-induced neoantigens broaden the immunotherapeutic window of cancers with low mutational loads Proceedings of the National Academy of Sciences of the United States of America. 2021;118.

39. Melero I, Berman DM, Aznar MA, Korman AJ, Perez Gracia JL, Haanen J. Evolving synergistic combinations of targeted immunotherapies to combat cancer. Nature reviews Cancer 2015;15:457–72. [PubMed: 26205340]

40. Engel FB, Schebesta M, Duong MT, Lu G, Ren S, Madwed JB, et al. p38 MAP kinase inhibition enables proliferation of adult mammalian cardiomyocytes. Genes & development 2005;19:1175–87. [PubMed: 15870258]

41. Su X, Esser AK, Amend SR, Xiang J, Xu Y, Ross MH, et al. Antagonizing Integrin beta3 Increases Immunosuppression in Cancer. Cancer research 2016;76:3484–95. [PubMed: 27216180]

42. Luo X, Fu Y, Loza AJ, Murali B, Leahy KM, Ruhland MK, et al. Stromal-Initiated Changes in the Bone Promote Metastatic Niche Development. Cell reports 2016;14:82–92. [PubMed: 26725121]

43. Zheng GX, Terry JM, Belgrader P, Ryvkin P, Bent ZW, Wilson R, et al. Massively parallel digital transcriptional profiling of single cells. Nat Commun 2017;8:14049. [PubMed: 28091601]

44. Ni Z, Chen S, Brown J, Kendziorski C. CB2 improves power of cell detection in droplet-based single-cell RNA sequencing data. Genome Biology 2020;21:137. [PubMed: 32513247]

45. McGinnis CS, Murrow LM, Gartner ZJ. DoubletFinder: Doublet Detection in Single-Cell RNA Sequencing Data Using Artificial Nearest Neighbors. Cell Systems 2019;8:329–37.e4. [PubMed: 30954475]

46. Stuart T, Butler A, Hoffman P, Hafemeister C, Papalexi E, Mauck WM 3, et al. Comprehensive Integration of Single-Cell Data. Cell 2019;177:1888–902.e21. [PubMed: 31178118]

47. Franzén O, Gan LM, Björkegren JLM. PanglaoDB: a web server for exploration of mouse and human single-cell RNA sequencing data. Database (Oxford). 2019;2019:baz046, 1–9. [PubMed: 30951143]

48. Zhou S, Huang YE, Liu H, Zhou X, Yuan M, Hou F, et al. Single-cell RNA-seq dissects the intratumoral heterogeneity of triple-negative breast cancer based on gene regulatory networks. Mol Ther Nucleic Acids 2021;23:682–90. [PubMed: 33575114]

49. Aran D, Looney AP, Liu L, Wu E, Fong V, Hsu A, et al. Reference-based analysis of lung single-cell sequencing reveals a transitional profibrotic macrophage. Nature Immunology 2019;20:163–72. [PubMed: 30643263]

50. Baccin C, Al-Sabah J, Velten L, Helbling PM, Grunschlager F, Hernandez-Malmierca P, et al. Combined single-cell and spatial transcriptomics reveal the molecular, cellular and spatial bone marrow niche organization. Nature cell biology 2020;22:38–48. [PubMed: 31871321]

51. Faccio R, Takeshita S, Zallone A, Ross FP, Teitelbaum SL. c-Fms and the alphavbeta3 integrin collaborate during osteoclast differentiation. The Journal of clinical investigation 2003;111:749–58. [PubMed: 12618529]

52. Secca C, Faget DV, Hanschke SC, Carneiro MS, Bonamino MH, de-Araujo-Souza PS, et al. IRF2BP2 transcriptional repressor restrains naive CD4 T cell activation and clonal expansion induced by TCR triggering. Journal of leukocyte biology 2016;100:1081–91. [PubMed: 27286791]

53. Grossman RL, Heath AP, Ferretti V, Varmus HE, Lowy DR, Kibbe WA, et al. Toward a Shared Vision for Cancer Genomic Data. The New England journal of medicine 2016;375:1109–12. [PubMed: 27653561]

54. Robinson MD, McCarthy DJ, Smyth GK. edgeR: a Bioconductor package for differential expression analysis of digital gene expression data. Bioinformatics 2010;26:139–40. [PubMed: 19910308]

55. Ellrott K, Bailey MH, Saksena G, Covington KR, Kandoth C, Stewart C, et al. Scalable Open Science Approach for Mutation Calling of Tumor Exomes Using Multiple Genomic Pipelines. Cell systems 2018;6:271–81 e7. [PubMed: 29596782]

56. Newman AM, Steen CB, Liu CL, Gentles AJ, Chaudhuri AA, Scherer F, et al. Determining cell type abundance and expression from bulk tissues with digital cytometry. Nature biotechnology 2019;37:773–82.

Statement of Significance

Immunotherapy is rarely effective in breast cancer. We dissected the metastatic tumor stroma, which revealed a novel therapeutic approach that targets the stromal p38MAPK pathway and creates an opportunity to unleash an immunologic response. Our work underscores the importance of understanding the tumor stromal compartment in therapeutic design.
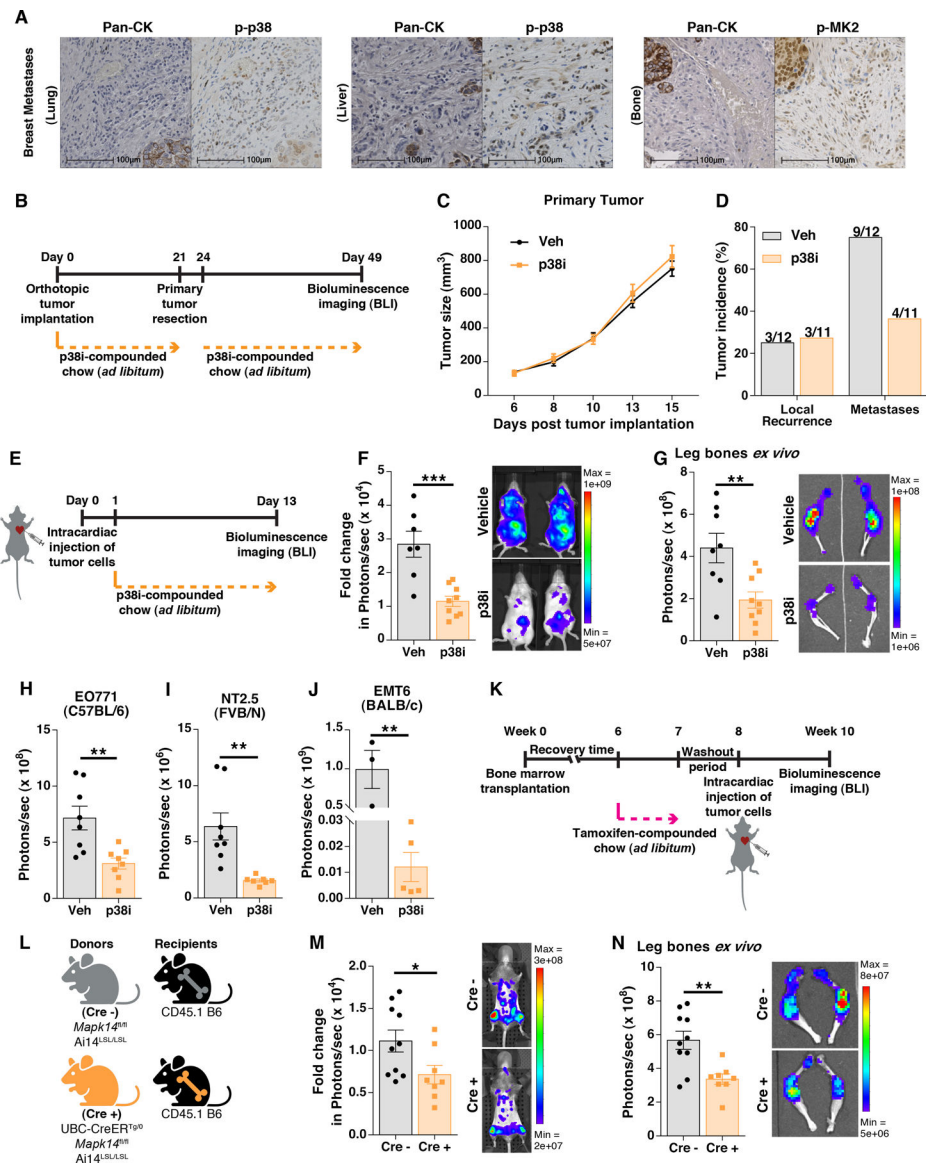
Figure 1. Hematopoietic stromal p38α supports metastatic tumor growth.
(A) Serial sections from human breast metastases were stained for cytokeratin (Pan-CK) and phospho-p38 (p-p38) or phospho-MK2 (p-MK2) by immunohystochemistry. Tumor stroma was identified by the absence of Pan-CK staining. **(B)** Luciferase-labeled (GFP-Luc) PyMT-BO1 breast cancer cells were implanted into the mammary fat pad and mice were treated as indicated. **(C)** Primary tumor growth was assessed by caliper measurements. **(D)** After primary tumor resection on day 21, disseminated tumor growth was assessed by bioluminescence imaging (BLI) on day 49. Vehicle (Veh), n=12; p38i, n=11). **(E, F, G, H, I, J)** Luciferase-labeled breast tumor cells were intracardically (i.c.) injected in the indicated mouse background. **(F)** PyMT-BO1 cells were i.c. injected in B6 albino mice. Disseminated metastatic tumor burden was measured by BLI on day 13 following tumor implantation. **(G)** Immediately after whole body measurements shown in F, leg bones were isolated and tumor burden was measured by ex vivo BLI. (n=7–9 biologically independent samples

per group). **(H)** Disseminated metastatic tumor burden for EO771 cells was measured by BLI on day 13 following i.c. implantation(n=8). **(I)** Disseminated metastatic burden for NT2.5 Her2/Neu cells was measured by BLI on day 13 following i.c. implantation (n=7–8). **(J)** Disseminated metastatic burden for EMT6 cells was measured by BLI on day 13 following i.c. implantation (n=3–5). **(K)** Bone marrow transplantation from CD45.2 UBC-CreERT2$^{cre/0}$*Mapk14*$^{fl/fl}$Ai14$^{LSL/LSL}$ and *Mapk14*$^{fl/fl}$Ai14$^{LSL/LSL}$ littermate donors to wildtype CD45.1 C57Bl/6 recipient mice was performed as shown in the schematics in (**L**). (Cre-, n=10; Cre+, n=8) **(M)** Transplanted mice were i.c. injected with luciferase-labeled PyMT-BO1 and disseminated tumor burden was assessed by BLI on day 14. **(N)** Immediately after BLI measurements shown in (**M**), leg bones were isolated and tumor growth assessed by ex vivo BLI. Unpaired student t test perfomed for all statistical analyses shown in this picture. All numerical data are represented as mean ± SEM. *, P<0.05; **, P<0.01; ***, P<0.001; ns, not significant.
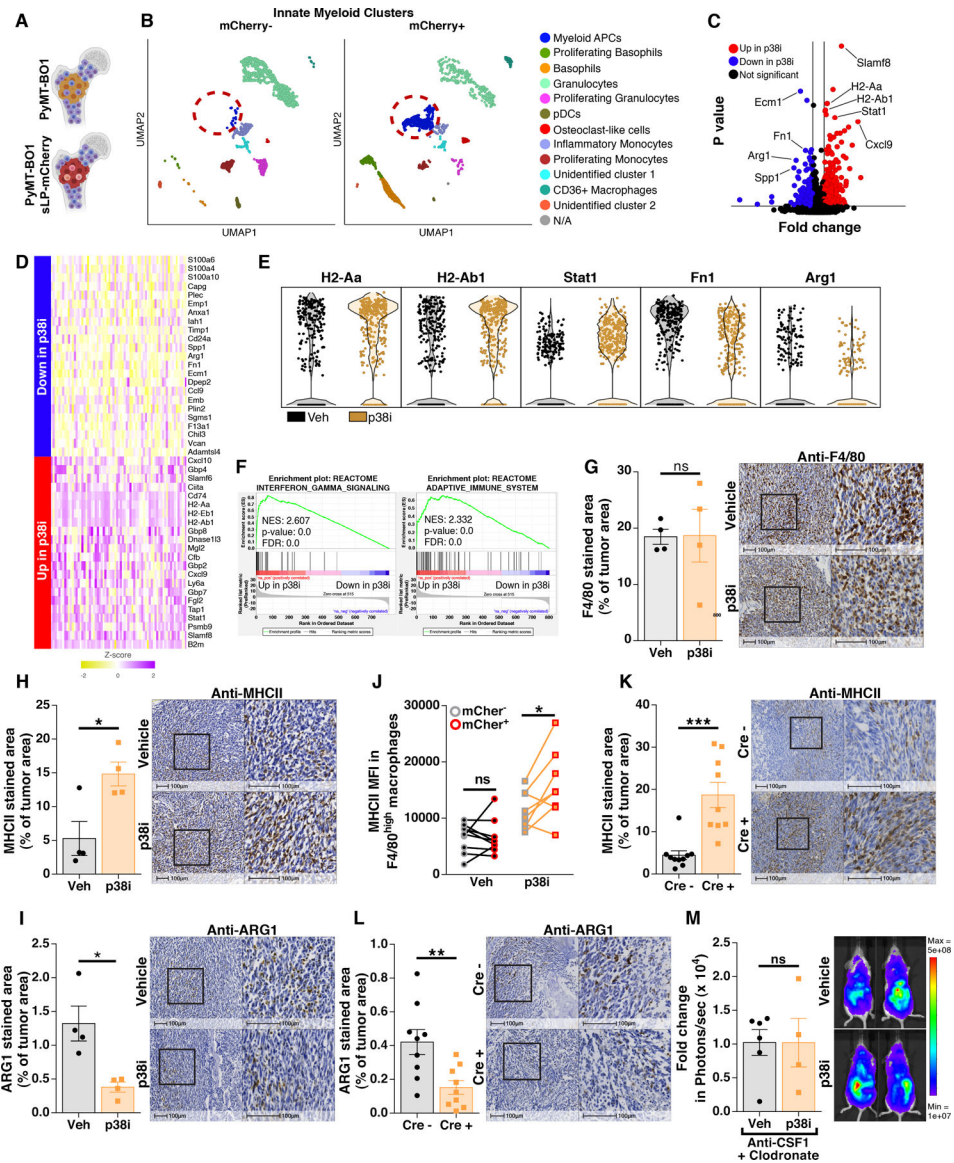
Figure 2. Inhibition of p38α signaling shifts tumor-associated macrophages from a tumor-promoting to a tumor-suppressive phenotype with increased IFNγ response signature.
(**A**) sLPmCherry-expressing tumor cells label tumor proximal stromal cells. These cells were used to isolate tumor proximal and distal stromal cells that were subjected to single cell RNA sequencing (scRNAseq) analyses. (**B**) Uniform Manifold Approximation and Projection (UMAP) of innate myeloid cells from pooled samples from each treatment condition segmented by mCherry status (n=4 per treatment; Total 4,880 cells; 1,220 cells per treatment condition/mCherry status after downsampling). (**C**) Volcano plot showing differential expression in tumor associated (mCherry+) myeloid APC clusters from each treatment condition found by scRNAseq analyses. Colored dots represent genes with statistically significant changes (p<0.05) and   1.5-fold change in expression levels in any direction. (**D**) Heatmap highlighing the most differentially expressed genes (23-downregulated; 22-upregulated) in tumor associated myeloid APCs upon p38i-treament. (**E**) Violin plots for selected genes showing differential expression levels in tumor-associated

(mCherry+) myeloid APCs found under vehicle and p38i-treated conditions. **(F)** Gene set enrichment analyses between tumor associated myeloid APCs found under vehicle versus p38i-treated conditions. Normalized Enrichment Score (NES), P-value and False Discovery Rate (FDR) are shown in the figure. **(G, H, I)** Immunohistochemical analyses were performed on tumor-bearing leg bones using F4/80 (**G**), MHCII (**H**) or ARG1 (**I**) specific antibodies. (n=4 biologically independent samples per group) **(J)** Flow cytometry analysis on gated F4/80^{high} macrophages from tumor-bearing femurs under vehicle and p38i-treated conditions. Lines connect data from the same mouse (n=8–9 biologically independent samples per group). **(K, L)** Immunohistochemical analyses were performed on tumor-bearing leg bones from mice shown in Fig 1M using MHCII (**K**) or ARG1 (**L**) specific antibodies (n=9–10 biologically independent samples per group). **(M)** PyMT-BO1 metastatic tumor burden was assessed upon macrophage depletion by BLI on day 13 after tumor cell implantation by i.c. injection. (n=4–6 biologically independent samples per group). Unpaired student t test perfomed for all statistical analyses shown in histological analyses and tumor burden quantification. Paired student t test performed for flow cytometry analyses shown in (J). All bar graph data are represented as mean ± SEM. *, P<0.05; **, P<0.01; ***, P<0.001; ns, not significant.
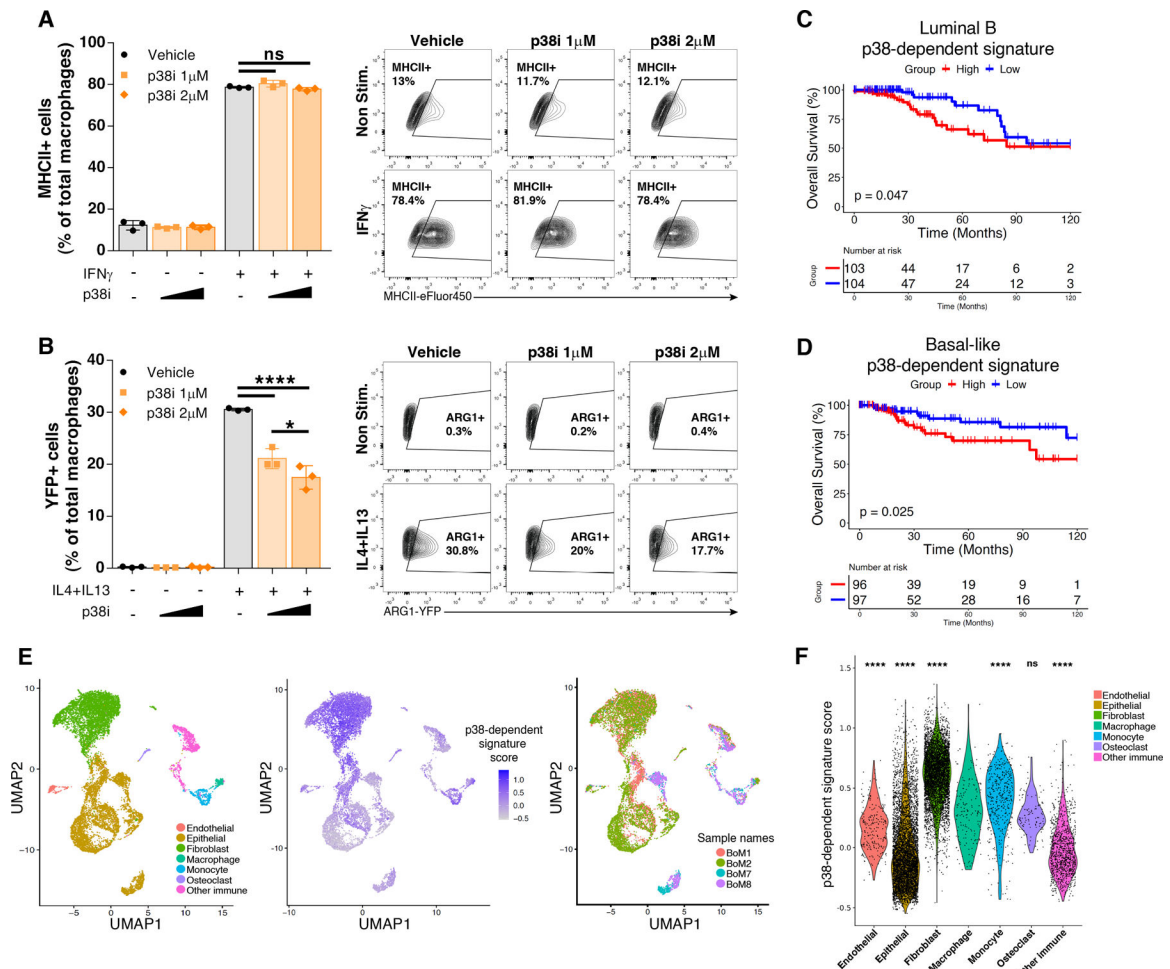
Figure 3. p38-dependent gene signature in primary breast tumors is associated with worse overall survival in human patients and is found in myeloid cells from human bone metastatic lesions.

(A, B) Bone-marrow derived macrophages isolated from the ARG1-YFP mouse were stimulated with 0.25U/ml of IFNγ (A) or IL4+IL13 20ng/ml (B) for 24 or 48 hours, respectively, in the presence or absence of increasing concentrations of p38i (n=3). Data are represented as mean ± SD. **(C)** Kaplan-Meier plot of overall survival of human luminal B breast cancer patients with high (red line) or low (blue line) p38-dependent gene signature (down in p38i, Fig 2D, S4B) using the TCGA database. **(D)** Kaplan-Meier (K-M) plot of overall survival of human basal-like breast cancer patients with high (red line) or low (blue line) p38-dependent gene signature (down in p38i, Fig 2D, S4B) using the TCGA database. **(E)** UMAP plot of bone metastases samples obtained from human patients. Cell types (left) identified based on canonial cell markers expression and SingleR automatic assignment, p38-dependent signature score (middle) calculated using Seurat AddModuleScore function and sample origin (right) are represented (n=4 samples obtained from 3 patients). **(F)** Violin plots for the p38-dependent gene signature score in the discriminated cell types from human bone metastases. One-way ANOVA with Tukey multiple comparisons test performed statistical analyses involving more than two groups in (A) and (B). Logrank test performed for K-M analyses. Wilcoxon test comparing macrophage population with other cell types

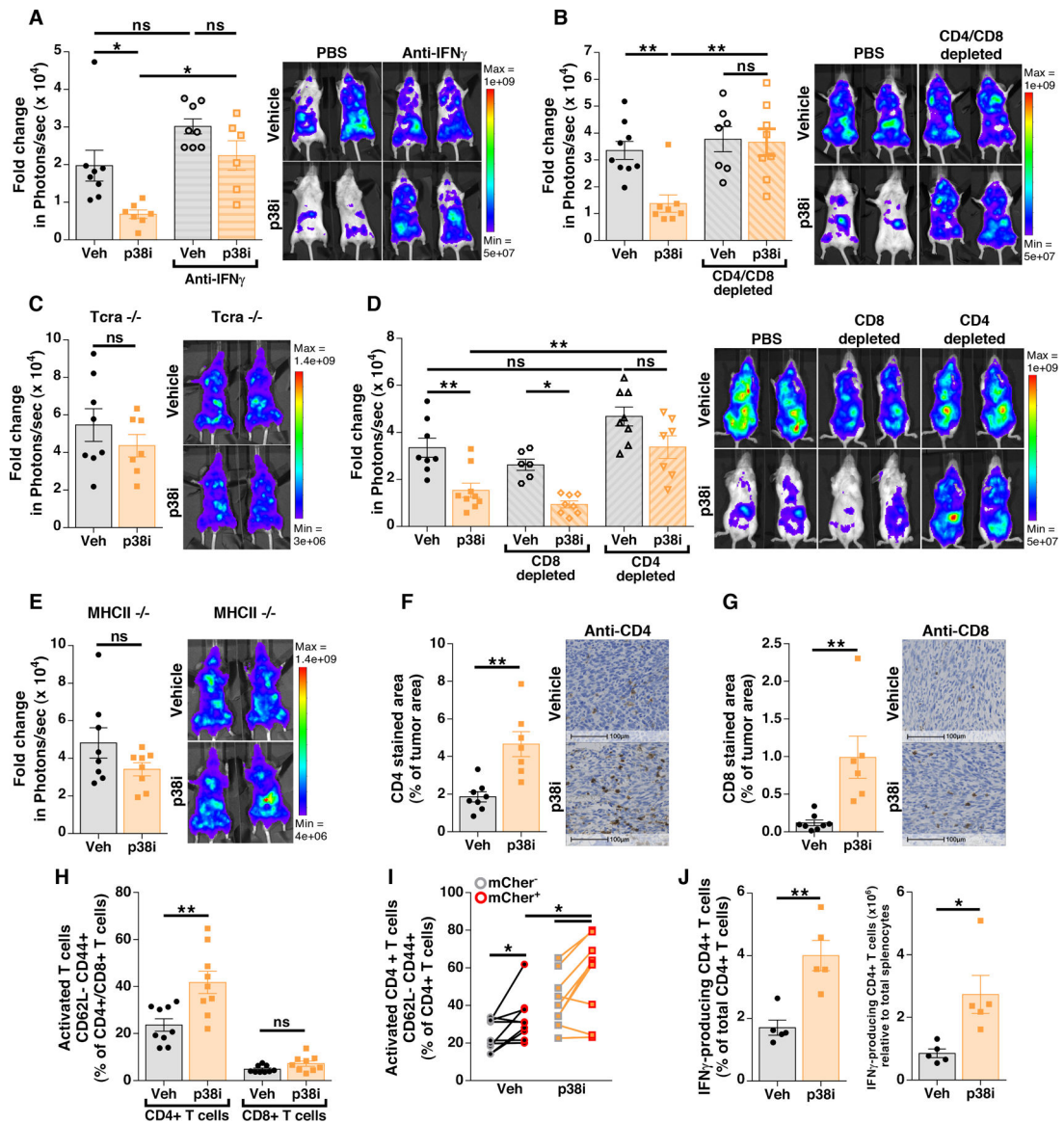was performed for the statistical analyses shown in (F). *, P<0.05; ****, P<0.0001; ns, not significant.

Figure 4. Inhibition of p38α reduces metastatic tumor growth in an IFNγ- and CD4+ T cell-dependent manner.

Mice were i.c. injected with PyMT-BO1 breast tumor cells, following the experimental design shown in Fig 1E, and disseminated metastatic tumor growth was assessed. (**A**) Quantification of BLI on day 13 (left) and representative images (right) upon IFNγ blockade. (**B**) Quantification of BLI on day 13 (left) and representative images (right) upon CD4+ and CD8+ T cell depletion. (**C**) Quantification of BLI on day 13 (left) and representative images (right) in Tcra–/– mice. (**D**) Quantification of BLI on day 13 (left) and representative images (right) in CD4+ or CD8+ T cell depleted mice. (**E**) Quantification of BLI on day 13 (left) and representative images (right) in MHCII–/– mice. n=7–9 biologically independent samples per group. (**F, G**) IHC analyses were performed on tumor-bearing leg bones using CD4 (**F**) or CD8 (**G**) antibodies. n=6–8 biologically independent samples per group. (**H**) Flow cytometry analyses of activated CD4+ and CD8+ T cells from tumor-bearing femurs. (**I**) Flow cytometry analyses of activated CD4+ T cells in bone

lesions from mice that were implanted with mCherry-labeled PyMT-BO1 tumor cells (n=9 biologically independent samples per group) **(J)** Splenocytes from tumor-bearing mice under vehicle or p38i treatment were isolated for *ex vivo* stimulation with PMA and ionomycin to assess IFNγ production (n=5 biologically independent samples per group). Estimated total numbers of IFNγ-producing CD4+ T cells in the spleen (right graph) were calculated by multiplying the frequency of IFNγ-producing CD4+ T cells found upon *ex vivo* stimulation and the total raw number of cells in the spleen from each treated mouse at the time of isolation. One-way ANOVA with Tukey multiple comparisons test performed all statistical analyses involving more than two groups. Unpaired student t test perfomed for statistical all analyses between two different treatment conditions. Paired student t test performed for analyses involving mCherry- and mCherry+ cells obtained from the same mouse. All bar graph data are represented as mean ± SEM. *, P<0.05; **, P<0.01; ns, not significant.
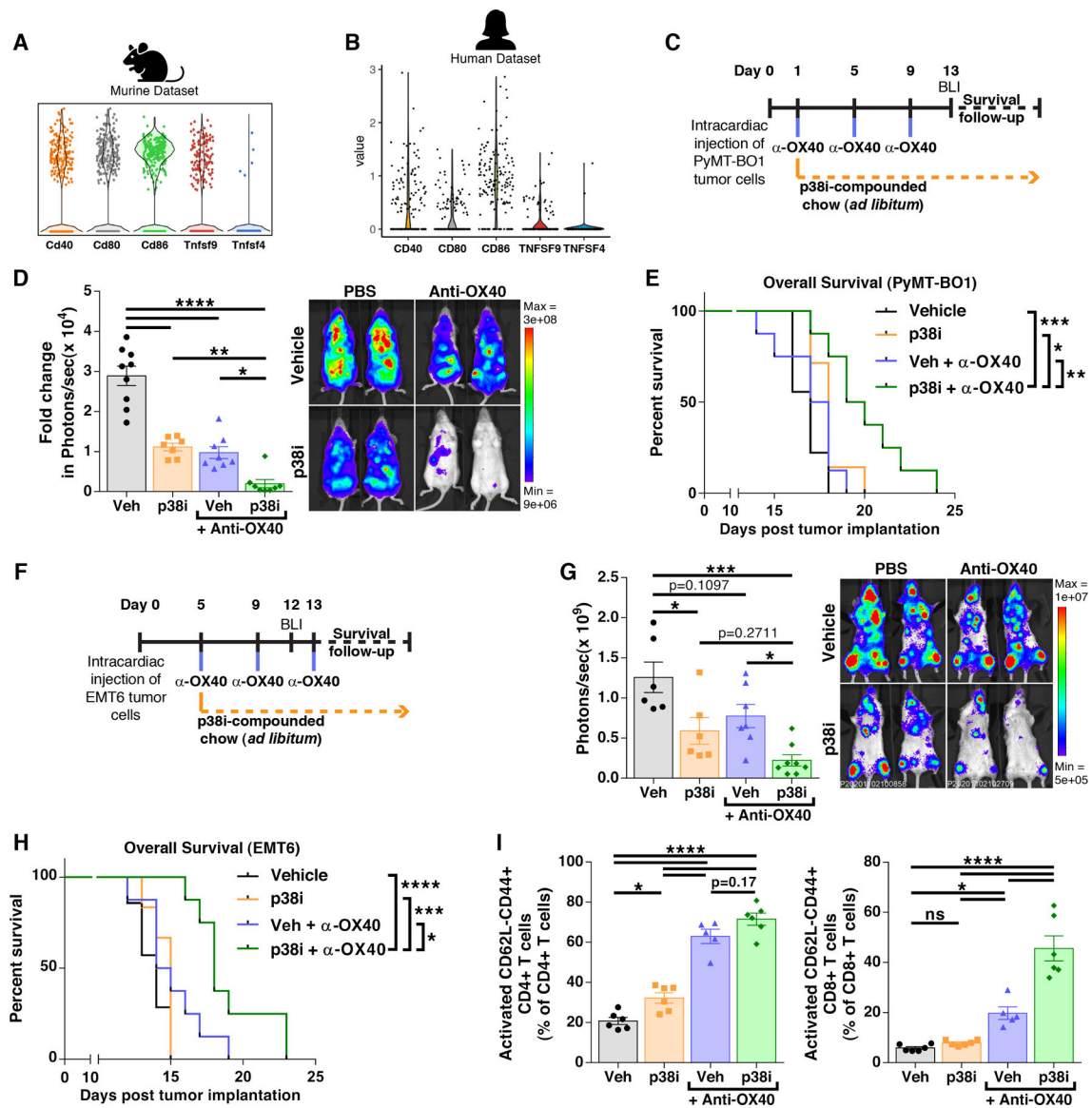
Figure 5. Inhibition of p38 synergizes with agonist anti-OX40 immunotherapy to reduce metastatic tumor growth.

(**A**) Violin plots for selected costimulatory genes in tumor-associated myeloid APC cluster from p38i-treated PyMT-BO1 bone metastases. (**B**) Violin plots for selected costimulatory genes in macrophages from human bone metastases. (**C**) PyMT-BO1 tumor cells were i.c. implanted and mice were treated as shown. (**D**) Disseminated metastatic growth of PyMT-BO1 tumors was measured on day 13 after tumor cell implatation by BLI (left) with representative pictures (right). (**E**) Overall survival of PyMT-BO1-implanted mice was assessed for up to 25 days. Vehicle, n=9; p38i, n= 7; anti-OX40, n=8; p38i+anti-OX40, n=8. (**F**) EMT6 tumor cells were i.c. implanted and mice were treated as shown. (**G**) Disseminated metastatic growth of EMT6 tumors was measured on day 12 after tumor cell implantation by BLI (left) with represenative pictures (right). (**H**) Overall survival of EMT6-implanted mice was assessed for up to 25 days. Vehicle, n=7; p38i, n= 6; anti-OX40, n=8; p38i+anti-OX40, n=8. (**I**) Flow cytometry analyses of activated CD4^{+} and CD8^{+} T

cells from PyMT-BO1 tumor-bearing femurs (n=5–6 biologically independent samples per group). One-way ANOVA with Tukey multiple comparisons test performed all statistical analyses involving more than two groups. Logrank test performed for overall survival analyses. All bar graph data are represented as mean ± SEM. *, P<0.05; **, P<0.01; ***, P<0.001; ****, P<0.0001; ns, not significant.
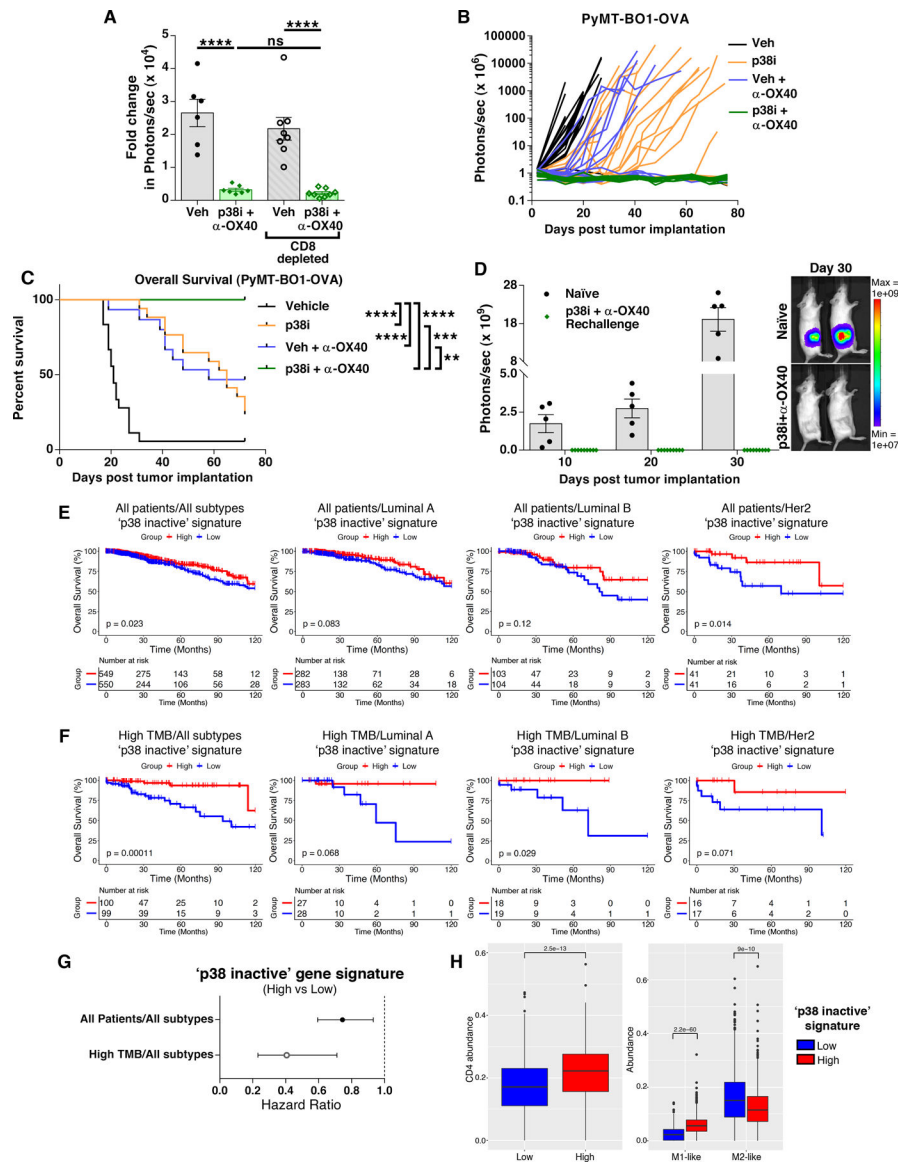
Figure 6. Neoantigenicity and 'p38 inactive' macrophage gene signature are associated with better overall survival in human breast patients.

(**A**) PyMT-BO1 metastatic tumor burden was assessed by BLI on day 13 after i.c. implantation under the combination treatment (p38i + anti-OX40) upon CD8$^+$ T cell depletion. (n=6–8 biologically independent samples per group) (**B**) OVA-expressing PyMT-BO1 tumor cells were i.c. implanted and mice treated as indicated in Fig. 5C and tumor burden was measured weekly for each mouse over 75 days. (**C**) Overall survival of mice implanted with OVA-expressing tumor cells was assessed for up to 75 days. Vehicle, n=18; p38i, n= 17; anti-OX40, n=15; p38i+anti-OX40, n=10. (**D**) Mice that underwent the combo treatment (p38i+ anti-OX40) in (C) were rechallenged with implantation of OVA-expressing PyMT-BO1 cells into the primary site and tumor growth was assessed by BLI (left) with representative images (right) at the indicated time. (**E**) Kaplan-Meier plots of overall survival of breast cancer patients with high (red line) or low (blue line) 'p38 inactive' gene signature segmented by selected subtypes using data from the TCGA database

(*n* is indicated on each plot; subtypes are indicated in the figure). **(F)** Kaplan-Meier plots of overall survival for breast cancer patients with high tumor mutational burden (TMB) segmented by high (red line) or low (blue line) 'p38 inactive' gene signature using the TCGA database (*n* is indicated on each plot; subtypes are indicated in the figure). **(G)** Hazard ratio plot of breast cancer patients with high 'p38 inactive' signature segmented by all patients or high TMB subset. **(H)** CD4$^+$ T cell, M1- and M2-like macrophage abundance was calculated by digital cytometry for high and low 'p38 inactive' human breast cancer samples from the TCGA database (p-values are shown in the figure). Log-rank test performed for K-M analyses. Cox analysis performed using 'p38 inactive' gene signature with patient age at diagnosis as covariate to produce hazard ratios.